A panchromatic spatially resolved analysis of nearby galaxies – I. Sub-kpc-scale main sequence in grand-design spirals

A. Enia [1,2]★ G. Rodighiero,[1,2] L. Morselli [1,2] V. Casasola,[3,4] S. Bianchi [4]
L. Rodriguez-Muñoz [1,2] C. Mancini [1,2] A. Renzini [2] P. Popesso,[5] P. Cassata,[1,2]
M. Negrello[6] and A. Franceschini[1]

[1]*Dipartimento di Fisica e Astronomia, Università di Padova, vicolo dell'Osservatorio 3, I-35122 Padova, Italy*
[2]*INAF – Osservatorio Astrofisico di Padova, vicolo dell'Osservatorio 5, I-35122 Padova, Italy*
[3]*INAF – Istituto di Radioastronomia, Via P. Gobetti 101, I-40129 Bologna, Italy*
[4]*INAF – Osservatorio Astrofisico di Arcetri, Largo E. Fermi 5, I-50125 Firenze, Italy*
[5]*Excellence Cluster Universe, Boltzmannstrasse 2, D-85748 Garching bei Munchen, Germany*
[6]*School of Physics and Astronomy, Cardiff University, The Parade, Cardiff CF24 3AA, UK*

ABSTRACT

We analyse the spatially resolved relation between stellar mass ($M_\star$) and star formation rate (SFR) in disc galaxies (i.e. the main sequence, MS). The studied sample includes eight nearby face-on grand-design spirals, e.g. the descendant of high-redshift, rotationally supported star-forming galaxies. We exploit photometric information over 23 bands, from the UV to the far-IR, from the publicly available DustPedia data base to build spatially resolved maps of stellar mass and SFRs on sub-galactic scales of 0.5–1.5 kpc, by performing a spectral energy distribution fitting procedure that accounts for both the observed and obscured star formation processes, over a wide range of internal galaxy environments (bulges, spiral arms, and outskirts). With more than 30 000 physical cells, we have derived a definition of the local spatially resolved MS per unit area for discs, $\log(\Sigma_{SFR}) = 0.82\log(\Sigma_*) - 8.69$. This is consistent with the bulk of recent results based on optical IFU, using the Hα line emission as an SFR tracer. Our work extends the analysis at lower sensitivities in both $M_\star$ and SFR surface densities, up to a factor of $\sim$10. The self-consistency of the MS relation over different spatial scales, from sub-galactic to galactic, as well as with a rescaled correlation obtained for high-redshift galaxies, clearly proves its universality.

Key words: galaxies: evolution – galaxies: spirals – galaxies: star formation.

1 INTRODUCTION

Galaxies appear to build their stellar masses in a steady mode mainly dominated by secular processes and thanks to the accretion of cold gas. This picture finds its confirmation in the existence of a tight relation between the galaxy stellar mass ($M_\star$) and its star formation rate (SFR): the main sequence (MS) of star-forming galaxies (SFGs), observed up to $z \sim 6$ with a fairly constant scatter of $\sim$0.3 dex (e.g. Daddi et al. 2007; Elbaz et al. 2007; Noeske et al. 2007; Pannella et al. 2009; Santini et al. 2009; Oliver et al. 2010; Rodighiero et al. 2014; Sobral et al. 2014; Speagle et al. 2014; Steinhardt et al. 2014; Whitaker et al. 2014; Renzini & Peng 2015; Schreiber et al. 2015; Shivaei et al. 2015; Santini et al. 2017; Pearson et al. 2018; Popesso et al. 2019a). Galaxies seem to oscillate around the MS relation as a consequence of multiple events of

central compaction of gas followed by inside-out gas depletion, thus related with the flows of cold gas in galaxies (Tacchella et al. 2016). Several works in the recent years exploited the MS relation as a reference to understand the differences among galaxies characterized by different rates of stellar production (starbursts, SFGs, and passive galaxies), with the final aim of understanding the origins of galaxy bimodality, and how the star formation activity is quenched (e.g. Rodighiero et al. 2011; Peng, Maiolino & Cochrane 2015; Saintonge et al. 2016).

The existence of a tight relation between stellar mass surface density ($\Sigma_\star$) and SFR surface density (Σ_{SFR}) found in H II regions of nearby galaxies, suggested that the global MS relation originates thanks to local processes that set the conversion of gas into stars (Rosales-Ortega et al. 2012; Sánchez et al. 2013). Such observations were complemented by the work of Wuyts et al. (2013), who discovered a correlation between $\Sigma_\star$ and Σ_{SFR} on scales of 1 kpc in galaxies at $0.7 < z < 1.5$ thanks to the combination of multi-wavelength broad-band imaging from the Cosmic Assembly Near-

infrared Deep Extragalactic Legacy Survey (Grogin et al. 2011; Koekemoer et al. 2011) and 3DHST data (Brammer et al. 2012).

Following this, several works exploited the advent of large integral field spectroscopic (IFS) surveys to analyse the existence of a spatially resolved MS relation at low redshifts, using the Hα flux as an SFR tracer. Cano-Díaz et al. (2016) used the Calar Alto Legacy Integral Field Area Survey (CALIFA; Sánchez et al. 2012) galaxies and found a spatially resolved MS on 0.5–1.5 kpc scales with a slope of 0.72 ± 0.04 and a scatter of 0.23 dex. Hsieh et al. (2017) identified H II spaxels in MaNGA (Mapping Nearby Galaxies at APO; Bundy et al. 2015) SFGs and found a linear resolved MS on kpc scales with a scatter of 0.127. These results suggest that the global relation is set locally, possibly by the surface density of molecular gas (Lin et al. 2017). Exploiting pixel-by-pixel spectral energy distribution (SED) fitting, Abdurro'uf (2017) analysed the spatially resolved MS in a sample of 93 local massive galaxies on ∼kpc scales. They find that the slope of the relation varies dramatically (from 0.3 to 0.99) depending on the range of $\Sigma_\star$ used for fitting, somehow recalling the bending of the MS observed in the integrated MS relation (e.g. Popesso et al. 2019a). In addition, they find a scatter that varies between 0.55 and 0.7 and that they ascribe to a combination of local variations of the specific SFR and different large-scale galaxy properties (i.e. morphology, and existence of a bar). Jafariyazani et al. (2019) found a spatially resolved MS in galaxies at $0.1 < z < 0.42$ observed with MUSE. Medling et al. (2018) estimated the MS from ∼800 galaxies in the Sydney AAO Multi-object Integral Field Galaxy Survey (SAMI; Croom et al. 2012) at $z < 0.1$, finding a slope of 1.0. Hall et al. (2018) studied the spatially resolved MS in a sample of 93 nearby galaxies drawn from the Survey for Ionized Neutral Gas in Galaxies (SINGG; Meurer et al. 2006) and the Wide-field Infrared Survey Explorer (WISE; Wright et al. 2010) on scales ranging from 50 pc to 10 kpc. They find that the slope, scatter, and normalization of the relation do not vary when changing the spatial scale, up to 1–1.5 kpc. They also find no dependence of the scatter (of both the spatially resolved and the global relation) on structural parameters of galaxies (morphology) and their H I gas fraction (as previously suggested for the global MS by, e.g. Saintonge et al. 2016). Thus, they conclude that the MS scatter can be driven by systematic differences in the star formation process among galaxies or their global environment. Cano-Díaz et al. (2019) exploited a sample of 2000 MaNGA galaxies to study the global and spatially resolved MS and its dependence on morphology. They find a spatially resolved MS with a slope close to 1 and a scatter of 0.27 dex, around which SF areas are located depending on the galaxy integrated morphology. They conclude that some processes related to morphology must set the local SF activity of a galaxy. Recently, Vulcani et al. (2019) studied the spatially resolved MS in a sample of 30 local late-type SFGs up to four effective radii, exploiting the GAs Stripping Phenomena in galaxies with the MUSE survey (Poggianti et al. 2017). They find that $\Sigma_\star$ and Σ_{SFR} correlate with a scatter of 0.3 dex, larger than the one observed for CALIFA and MaNGA galaxies. Interestingly, this correlation is found to vary dramatically when studied for single galaxies: For several sources a correlation is not even present, for others multisequences are observed, undermining the existence of a universal correlation.

To reconcile and homogenize all these observational results into a coherent scenario, it is mandatory to account for the different selection samples and for potential systematics in the methodology adopted to compute the galaxy physical parameters. To this aim, we try to cope with the main biases affecting the bulk of the previous works that are almost based on emission lines (i.e. Hα) or UV-to-optical tracers to constrain the SFR (see Sanchez et al. 2019, for a

review). Here, we exploit the power of a complete multiwavelength photometric coverage, extending from the far-UV (FUV) up to the far-IR (i.e. from *GALEX* to *Herschel*) to provide a reliable measure of the comprehensive SFR in galaxies, directly accounting for both the observed and obscured components. This is obtained by performing an SED fitting procedure, which, accounting for an energetic balance, allows us to go deeper than spectroscopic surveys based on Hα emission lines. The latter critically depend on dust extinction corrections derived from the Balmer decrement and mostly on the spectral signal-to-noise ratio (SNR) limit needed (for example) for the spaxel classification on BPT diagrams, requiring significant detection of four emission lines. Thus, we exploit the higher SNR of the photometric data that allows us to reach the farthest galactocentric distances, and the combination of UV and far-infrared (FIR) measurements to minimize the uncertainties related to the presence of dust.

With such a machinery, in this work (Paper I) we aim at defining the MS at kpc-scales in a sample of nearby face-on spirals collected in DustPedia (Davies et al. 2017). This choice is driven by the need to first characterize the final products of pure secular evolution processes, i.e. unperturbed discs, that have assembled at earlier cosmic epochs the bulk of the stars that we observe in today's galaxies (Rodighiero et al. 2011; Sargent et al. 2012). Indeed, grand-design spiral galaxies are considered to account for the largest percentage of SFGs sitting on the local MS (Wuyts et al. 2011; Morselli et al. 2017). This work focuses first on the study of typical MS systems and it will be extended in the future to other morphological-type galaxies, which are statistically located at larger distances from the local relation. To reach a comprehensive picture on the star formation process in galaxies, in a companion paper (Paper II, Morselli et al. in prep.) we will investigate possible variations of the star formation efficiency within galaxies, as well as the relation between cold gas availability and SFR.

The paper is structured as follows. In Section 2 we describe the data set. In Section 3 we present our SED fitting methodology (e.g. libraries and image processing). In Section 4 we present our results on the spatially resolved MS. Throughout the paper, we will assume a ΛCDM cosmology (Planck Collaboration XIII 2016) and Chabrier (2003) IMF.

2 DATA AND SAMPLE

We exploit the vast amount of data from DustPedia,[1] a collection of more than 875 local galaxies, built with the purpose of studying the dust emission in the local Universe. DustPedia comprises every *Herschel* observed galaxy within ∼50 Mpc from the Milky Way, with a diameter $D_{25} > 1$ arcmin. The multiwavelength photometric data presented in DustPedia have been homogenized, making this data set particularly interesting for our purposes.

2.1 Sample selection

Starting from the DustPedia collection, we build a coherent sample of local SFGs with a 'grand-design spiral' structure. Thus, we select galaxies having a Hubble stage index T (or RC3 type; de Vaucouleurs et al. 1991; Corwin, Buta & de Vaucouleurs 1994) between 2 and 8, and a diameter $D_{25} > 6$ arcmin. To avoid complications related to disc inclination (i) and dust correction, we focus here on nearly face-on sources with $i < 40°$. Furthermore, we

---

[1]The DustPedia website is available at http://dustpedia.astro.noa.gr.

Table 1. Our galaxy sample. Galaxy name, coordinates in J2000 system reference, distances D (in Mpc), inclinations, r_{25} sizes (the semimajor axis isophote at which the optical surface brightness falls beneath 25 mag arcsec^{-2}), and morphological classifications are the same adopted by the DustPedia collaboration, and come from the HyperLEDA data base (Makarov et al. 2014). The values of $M_\star$ and SFR are obtained by fitting the DustPedia photometry with MAGPHYS, the former as the standard MAGPHYS output, and the latter from the scaling relations in equations (1) and (2). It is worth noticing that NGC 5194 aperture photometry comprehends both fluxes coming from M51a and M51b. Reported cell sizes are referred to the so-called *pixel-by-pixel* SED fitting (in this case, with 8 arcsec square size, reported in kpc) and regions probing a fixed physical scale (1.5 kpc, in arcseconds), as reported in Section 3.

| Galaxy name | RA | DEC | D | i | r_{25} | $\log M_\star$ | SFR | Cell size | | RC3 type |
| | | | | | | | | 8 arcsec | 1.5 kpc | |
	(deg)	(deg)	(Mpc)	(°)	(kpc)	(M$_\odot$)	(M$_\odot$ yr^{-1})	(kpc)	(arcsec)	
NGC 0628 (M74)	24.1740	15.7833	10.14	19.8	14.74	10.41 ± 0.15	1.90 ± 0.41	0.39	30.60	Sc
NGC 3184	154.5708	41.4244	11.64	14.4	12.55	10.14 ± 0.10	0.98 ± 0.10	0.45	26.67	SABc
NGC 3938	178.2057	44.1208	19.41	14.1	10.04	10.16 ± 0.20	2.19 ± 0.19	0.75	16.03	Sc
NGC 4254 (M99)	184.7065	14.4164	12.88	20.1	9.40	10.02 ± 0.18	2.44 ± 0.23	0.50	24.11	Sc
NGC 4321	185.7282	15.8219	15.92	23.4	14.30	10.74 ± 0.15	3.27 ± 0.37	0.62	19.52	SABb
NGC 4535	188.5845	8.1978	14.93	23.8	17.62	10.19 ± 0.19	1.30 ± 0.08	0.58	20.81	Sc
NGC 5194 (M51)	202.4695	47.1952	8.59	32.6	17.23	10.70 ± 0.20	4.08 ± 0.26	0.33	36.10	Sbc
NGC 5457 (M101)	210.8025	54.3491	7.11	16.1	24.81	10.38 ± 0.13	2.48 ± 0.15	0.28	43.60	SABc

apply a cut-off in distance (around 1000 km s^{-1}, corresponding to approximately 22 Mpc), as for galaxies beyond this distance the sub-mm photometry is scarcely resolved or even below the observational beam. Finally, to robustly estimate the physical parameters of galaxies from SED fitting, we restrict our analysis to those having a uniform coverage in the wavelength domain, with at least 20 bands of observation.

The final sample includes eight objects: NGC 0628, NGC 3184, NGC 3938, NGC 4254, NGC 4321, NGC 4535, NGC 5194, and NGC 5457. Distances, sizes, inclinations, and morphologies are those adopted by the DustPedia collaboration, based on the HyperLEDA data base[2] (Makarov et al. 2014), and are available on their website (see Table 1). The sample stellar masses are in the range between 10^{10} and 10^{11} M$_\odot$, and SFRs are between 1 and 4 M$_\odot$ yr^{-1}. These sources represent the evolved descendants of high-redshift normal SFGs, which are rotationally supported systems, at least by $z = 2$ (e.g. Förster Schreiber et al. 2009, 2018; Wisnioski et al. 2015). Moreover, their regular dynamical properties suggest that they have quiescently assembled their stellar mass through cosmic times. In Fig. 1 we present, as an example, the galaxy NGC 0628 as it is observed in the FUV with the *GALaxy Evolution eXplorer* (*GALEX*; Morrissey et al. 2007), in the *g* band with the Sloan Digital Sky Survey (SDSS; York et al. 2000), in the *J* band with the 2 Micron All-Sky Survey (2MASS; Skrutskie et al. 2006), at 8 μm with the *Spitzer Space Telescope* (Werner et al. 2004), at 12 μm with WISE, and finally at 250 μm with the *Herschel Space Observatory* (Pilbratt et al. 2010). In the following paragraphs, we briefly report information on the different data sets used in this work. For a more systematic and complete reference about data reduction and processing (implemented by the DustPedia collaboration), we refer the reader to Clark et al. (2018).

2.2 *GALEX*

The ultraviolet part of the electromagnetic spectrum is sampled by *GALEX*. The *GALEX* data are divided in near-UV [NUV; 1516 Å, with full width at half-maximum (FWHM) of ∼4.25 arcsec] and FUV (2267 Å and ∼5.25 arcsec beam). NUV and FUV data are available for every galaxy in our sample, and sample the light

coming from newborn massive stars, tracing the unobscured star formation activity of galaxies.

2.3 SDSS

The optical part of the spectrum, sampling the young stellar content, is probed with the Data Release 12 of SDSS. We use five bands (*u*, *g*, *r*, *i*, and *z*), with effective wavelengths of 3351, 4686, 6166, 7480, and 8932 Å, respectively. The SDSS FWHM varies from observation to observation, with a typical median value of 1.43 arcsec.

2.4 2MASS

Near-infrared (NIR) imaging comes from 2MASS in three bands, *J* band (1.25 μm), *H* band (1.65 μm), and K_s band (2.16 μm), with FWHMs between ∼2.5 and 2.7 arcsec. As noted in appendix D of Clark et al. (2018), 2MASS-*H*-band photometry might be affected by a particular offset with respect to *J*- and K_s-band photometry, translating as a 'bump' or 'dip' in the SED of the object. We find this problem only in NGC 0628 photometry, for which we exclude the *H*-band data point from the SED fitting.

2.5 WISE and *Spitzer*

The NIR and medium-infrared (MIR) parts of the spectrum are observed with the WISE and the IRAC camera onboard of *Spitzer*. WISE provides observations at 3.4, 4.6, 12, and 22 μm, with point spread function (PSF) FWHMs ranging from 5.70 to 11.8 arcsec. The IRAC camera, instead, collects observations at 3.56, 4.51, 5.76, and 8.00 μm, with a PSF FWHM varying between 1.66 and 1.98 arcsec. These bands are available for the whole sample, except for NGC 4535 and NGC 5457, both lacking 5.8 μm data. NIR and MIR observations trace the old stellar component, the stellar mass distribution, and the carbonaceous-to-silicate materials in the dust.

2.6 *Herschel*

Emission from the FIR to the sub-mm is observed with the instruments onboard the *Herschel Space Observatory*. We used both *Herschel* PACS (70, 100, and 160 μm) and SPIRE data (250 and 350 μm), with PSF FWHM of ∼6, 8, 12, 18, and 24 arcsec, respectively. The only exceptions are NGC 4535 and NGC 5194,

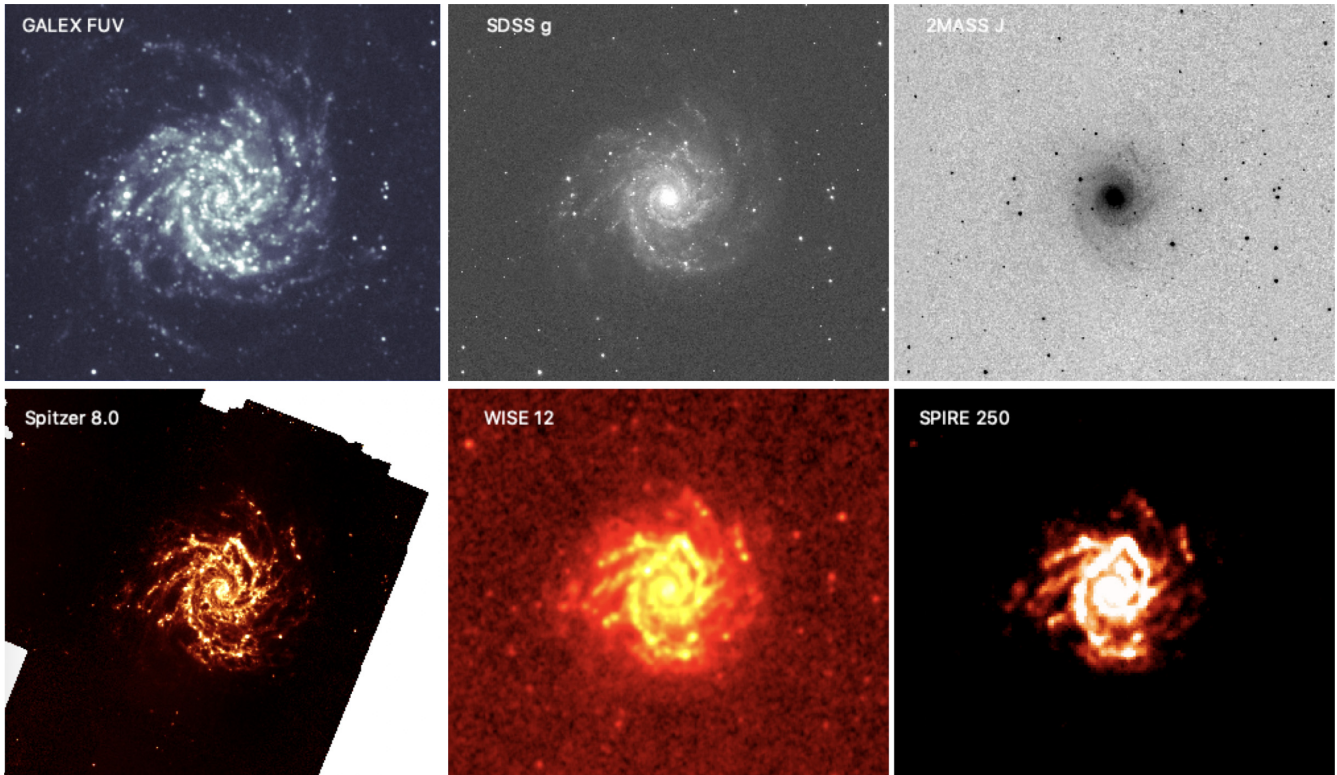[2]The HyperLEDA data base is available at http://leda.univ-lyon1.fr/.

Figure 1. Example of the multiwavelength imaging available for NGC 0628, coming from the DustPedia archive. Image size is ∼8 arcmin × 8 arcmin.

lacking 70 and 100 µm observations, respectively. These wavelengths typically probe the reprocessed emission coming from dust, and thus could constrain the dust-obscured star formation processes. We do not include the 500 µm channel in our SED fitting procedure. Indeed, in our approach (see Section 3) we need to downgrade all images to the lower resolution available in our maps. With a beam of ∼35 arcsec, the 500 µm does not allow us to push our spectro-photometric analysis to the kpc scale. However, we have verified that the performed SED best fits are consistent with the observed 500 µm flux densities. The adopted spatial scale for our analysis will be discussed in detail in Section 3.

3 METHODOLOGY AND SED FITTING

To obtain the spatially resolved physical properties of galaxies, like their stellar mass ($M_\star$) and SFRs, we perform an SED fitting on scales varying from 0.28 to 1.5 kpc.

Our procedure includes three steps: (i) matching the PSF of every image to the worst one, by degrading every band to the PSF of the SPIRE 350 image; (ii) building a grid of square cells of a given size and measuring the flux at each wavelength on them; (iii) deriving the physical properties of the individual cells by performing SED fitting to the available photometry.

We analyse each galaxy at two different resolutions: the first by considering cells of 8 arcsec × 8 arcsec (thus a varying length side in physical scale from one galaxy to another, as reported in Table 1), that is the pixel scale of SPIRE 350 maps, corresponding to three spaxels per resolution element, and the second by constructing fixed size cells of 1.5 kpc × 1.5 kpc, as this is the typical physical scale sampled in most of the literature. This is done to compare the reliability of the SED fitting procedure and the final results obtained sampling different spatial scales.

Finally, we also perform SED fitting on the integrated galaxy photometry coming from the DustPedia Photometric sample. This information is crucial to validate our photometric analysis (comparing with the public integrated properties of the DustPedia sample), and to understand the regulation of star formation properties on galactic scales as compared to sub-galactic scale, which is the main aim of this work. We also checked that the DustPedia integrated photometry is compatible with the one we obtain within the same apertures.

3.1 Image pre-processing and PSF degradation

As reported in Section 2, the starting point is the different photometric observations of the galaxies, downloaded from the DustPedia Archive. These have already been homogenized in flux, given in Jy, and World Coordinate System. For our purposes, on each map we perform: foreground star removal, background estimation, flattening and subtraction, and PSF degradation, matching the maps' resolution to the worst one.

Foreground star removal is performed exploiting the Comprehensive and Adaptable Aperture Photometry Routine (CAAPR) routine presented in Clark et al. (2018). The routine uses the PTS toolkit for SKIRT (Camps & Baes 2015) to detect and remove/patch foreground star emission, thus creating a star subtracted version of the map. As CAAPR sometimes mistakenly identifies bright H II regions as stars, we carefully visual-check the star-subtracted maps to be sure that only foreground stars are removed.

In each photometric band, we perform background estimation and subtraction on the star-subtracted maps. This procedure follows the indications in Clark et al. (2018), performing (if needed) a sky flattening fitting with a fifth-order polynomial 2D array, and then subtracting the background emission. This step is crucial to remove

Galactic foreground emission and to smooth out residual image gradients typical of some bands (i.e. *GALEX* and *Spitzer*).

Finally, we degrade the stars and background-subtracted maps to the PSF of SPIRE 350. To do this, we convolve the maps using the kernels provided by Aniano et al. (2011),[3] in order to match each band to the PSF of SPIRE 350.

3.2 Spatially resolved SED fitting

To perform SED fitting, we measure the flux in each photometric band inside the cells with the PHOTUTILS V0.6 Python package (Bradley et al. 2019). Then, we correct all the fluxes with wavelength lower than 10 μm for Galactic extinction, with the in-built module in CAAPR, based on values in the IRSA Galactic Dust Reddening and Extinction Service. To estimate errors on the flux, we apply the following procedure. When available, we use the error maps in the DustPedia Archive (i.e. *Spitzer* bands and the far-IR photometry). If no error map is available (i.e. the SDSS maps), we take the SNR of the DustPedia Photometry in that particular band (accounting also for calibration error), and use that to evaluate the error in each cell [this is different from what was done by Smith & Hayward (2018), who adopt a default SNR of 5 for every band]. As a result, we obtain two photometric catalogues (for the 8 arcsec × 8 arcsec cell and for the 1.5 kpc × 1.5 kpc cell) containing the flux in every available photometric band from UV to far-IR, the relative errors, and the associated astrometric positions of the pixel/cell centres. We include in the SED fitting procedure only cells with no more than five undetected bands. The discarded cells are mostly found in the outermost part of galaxies. This cut critically reduces the total computational time of the subsequent SED fitting procedure.

To perform SED fitting, we use the publicly available code MAGPHYS (da Cunha, Charlot & Elbaz 2008). MAGPHYS is one of the state-of-art codes to model panchromatic SED, and as such has been extensively used in the literature (e.g. da Cunha et al. 2010; Smith et al. 2012; Berta et al. 2013; Chang et al. 2015; Hayward & Smith 2015; Smith & Hayward 2015; Chrimes et al. 2018; Driver et al. 2018; Williams, Gear & Smith 2018; Martis et al. 2019). It simultaneously models the emission observed in the UV-to-FIR regime by consistently assuming that the whole energy output is balanced between the one emitted at UV/optical/NIR wavelengths that is absorbed by dust and the one re-emitted in the FIR. It does so exploiting a Bayesian approach to determine the posterior distribution functions of the parameters by fitting the observed photometry to the model emission coming from a set of native libraries within the MAGPHYS distribution. These libraries are composed of 50 000 stellar population spectra with varying star forming histories [described by a continuous model $\psi(t) \propto \exp^{-\gamma t}$ with superimposed random bursts] derived from the Bruzual & Charlot (2003) spectral library. Formation ages are uniformly distributed between 0.1 and 13.5 Gyr (thus, they are shorter or equal to the age of the Universe for the nearby galaxies in this work). The typical SF time-scales are uniform between 0 and 0.6 Gyr⁻¹, dropping exponentially around 1 Gyr⁻¹. Metallicities are taken from a uniform grid with values ranging between 0.02 and 2 $Z_\odot$. The stellar emission libraries are associated, via the energy balance criterion, to 50 000 two-component dust emission SEDs (Charlot & Fall 2000; da Cunha et al. 2008), accounting for the emission coming from the so-called stellar birth clouds and the diffuse interstellar medium. MAGPHYS has already been used to

model panchromatic SED of local galaxies (e.g. Viaene et al. 2014, for M31) and its ability to properly retrieve physical properties from the SED has been tested on hydrodynamical simulations of galaxies (i.e. isolated disc or major merger as in Hayward & Smith 2015; Smith & Hayward 2015) and of resolved regions (Smith & Hayward 2018). In particular, Smith & Hayward (2018) run MAGPHYS on 21 bands of a simulated isolated local disc galaxy, on regions spanning from 0.2 to 10 kpc, also with different disc inclinations, in order to test its ability to recover physical properties (such as $M_\star$, SFRs, and SFHs) and derived ones (i.e. metallicity and visual extinction A_V). They find that MAGPHYS is able to produce acceptable fits to almost every cell enclosed inside the *r*-band effective radius, and between 59 and 77 per cent of cells within 20 kpc from the centre (even though the SNR choice of 5 might play an important role in keeping the χ^2 total value below the threshold). Those fits lead to reasonably good parameter estimate for every built-in MAGPHYS output.

Following Smith & Hayward (2018), we input the measured fluxes to MAGPHYS for SED fitting. As anticipated in Section 3, we perform spatially resolved SED fitting for each galaxy using two different dimensions of the cell: 8 arcsec and 1.5 kpc. This is done for two reasons: (i) to compare the results on different spatial scales, and (ii) to test the reliability of the pixel-by-pixel SED analysis. In fact, the physical scales probed in this work vary from ∼280 pc for NGC 5457 (the closest galaxy in our sample) to ∼750 pc for NGC 3938 (the most distant; see Table 1). These scales are at the limit of the assumption on which the balance between star formation laws and energy output still holds (e.g. Kravtsov 2003; Schruba et al. 2010; Khoperskov & Vasiliev 2017). In Section 4 we show how the 8 arcsec results and the 1.5 kpc ones are consistent, thus concluding that our analysis is reliable also on the smallest scales.

To accept or reject a fit, we apply a criterion based on Hayward & Smith (2015), where they used a χ^2 threshold of 20 on 17 simulated photometric bands. Differently, in Smith & Hayward (2018) the threshold is set to 30.6 on 21 simulated bands. As the galaxies in our sample have been observed with 21 (NGC 4535) or 23 photometric bands, we use a conservative χ^2 cut of 25. χ^2 maps for each galaxy are reported in Fig. 2. The blue squares are the values below the threshold, while the red points are the rejected ones. In NGC 5194 the companion galaxy M51b has been removed by further rejecting each cell with a declination δ over 47.240 52. On average, each galaxy has ∼4000 accepted points, with the exceptions of the closest ones, NGC 5194 (∼10 000) and NGC 5457 (∼15 000).

3.3 Stellar mass and SFR estimates

The output of the SED fitting process is a wide range of physical properties. To probe the MS, the two fundamental quantities are the stellar mass and the SFR. $M_\star$ values are directly taken from the MAGPHYS output. SFRs are obtained by summing unobscured (SFR$_{UV}$) and obscured (SFR$_{IR}$) contributions. SFR$_{UV}$ is estimated using the relation of Bell & Kennicutt (2001):

$$\text{SFR}_{UV} = 0.88 \times 10^{-28} L_\nu, \tag{1}$$

where L_ν in erg s⁻¹ Hz⁻¹ is evaluated from the SED fit at 150 nm.

SFR$_{IR}$ is computed using the relation of Kennicutt (1998):

$$\text{SFR}_{IR} = 2.64 \times 10^{-44} L_{IR}, \tag{2}$$

where L_{IR} in erg s⁻¹ is evaluated from the SED fit between 8 and 1000 μm (rest frame). In both cases, the relations have been rescaled in accordance with a Chabrier (2003) IMF.

We evaluate the SFRs from empirical relations that are less model dependent rather than using the SFRs obtained from the SED fit that
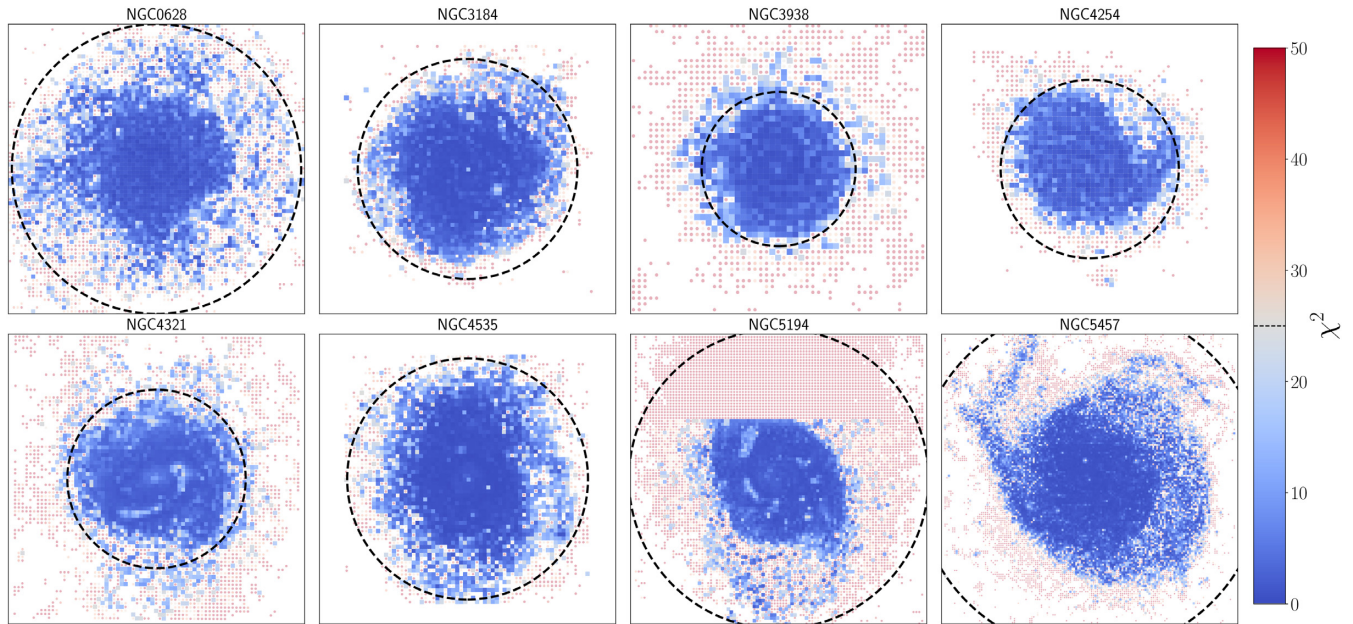
Figure 2. Final χ^2 maps for the full sample of galaxies for cells of 8 arcsec. The blue coloured squares are the accepted values (below the threshold of 25, highlighted with a dotted line in the colourbar), and the red shaded points are the discarded ones lying over the threshold. For NGC 5194, each point with $\delta >$ 47.240 52 has been discarded in order to remove contamination from the M51b companion (they form a second tight sequence below the accepted cells). The dotted circle is the galaxy r_{25} reported in Table 1. Almost every cell in the innermost galaxy regions is accepted. In the outer part of the disc, the spiral arms tend to produce acceptable fits with respect to the non-spiral part of the galaxies, as it is clear from NGC 5457.
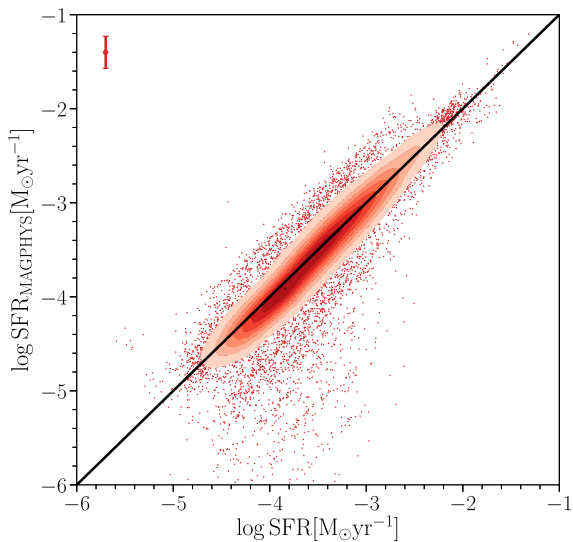
Figure 3. Comparison between the MAGPHYS output star formation rates (*y*-axis) and the ones we used throughout this work, obtained from empirical relations in equations (1) and (2) (*x*-axis). The red errorbar in the upper left highlights the median error on the measure. The black line is the 1:1 relation. The majority of the sample is consistent with this relation, and only a small fraction (2.34 per cent) see their SFR increase by more than one order of magnitude.

are more dependent on degenerate parameters like age, metallicity, and extinction. A comparison between the SFRs obtained from the empirical relations and the ones given as output of MAGPHYS is shown in Fig. 3. The scatter of the relation is relatively small, but the SFRs from MAGPHYS are, on average, ∼0.1 dex smaller than the ones from the empirical relations. A detailed comparison of the output values of MAGPHYS with those from other tools or

receipts is beyond the goal of this paper. However, we note that the SED fitting technique accounts for the contribution of different stellar populations at various ages, as determined by the assumed SFHs. The empirical approach adopted here (and widely used in the literature) accounts for the contribution of two extreme populations: the UV emission from young stars, and the totally obscured young stellar component still hidden in the dusty molecular clouds. The tight correlation found in Fig. 3 ensures that the use of the SFR from MAGPHYS would not change the results presented in the next section. There are some points falling below the 1:1 relation, 369 with SFR increased by an order of magnitude, and 134 by two orders of magnitude. This is due to attributed star forming activity to what the MAGPHYS models identify as (strong) diffuse cirrus emission in the spiral arms and in the inter-arms regions (the spatial distribution is Gaussian, centred on $0.5r/r_{25}$). Anyway, we stress that the impact of these points on the overall results is non-existent, being an extremely small fraction (1.72 and 0.62 per cent, respectively) of the full sample.

4 RESULTS

Before deriving any general conclusions and implications from the statistical analysis of the combined sample of local face-on spirals introduced in this work, we briefly present the main results about each individual source. An example for NGC 0628 is shown in Fig. 4 (the others are in Appendix A). In these figures, we present for each source: the maps of SFR, stellar mass, and distance from the MS (Δ_{MS} evaluated as the perpendicular distance of a point in the $\log \Sigma_\star - \log \Sigma_{SFR}$ from the MS relation), using as reference the MS evaluated for the combined sample), as well as the distribution of the cells in the $\log \Sigma_\star - \log \Sigma_{SFR}$ plane, colour coded as a function of the distance of the cell from the galaxy centre, in units of r_{25}. The dots in the maps correspond to rejected cells (with χ^2 larger than
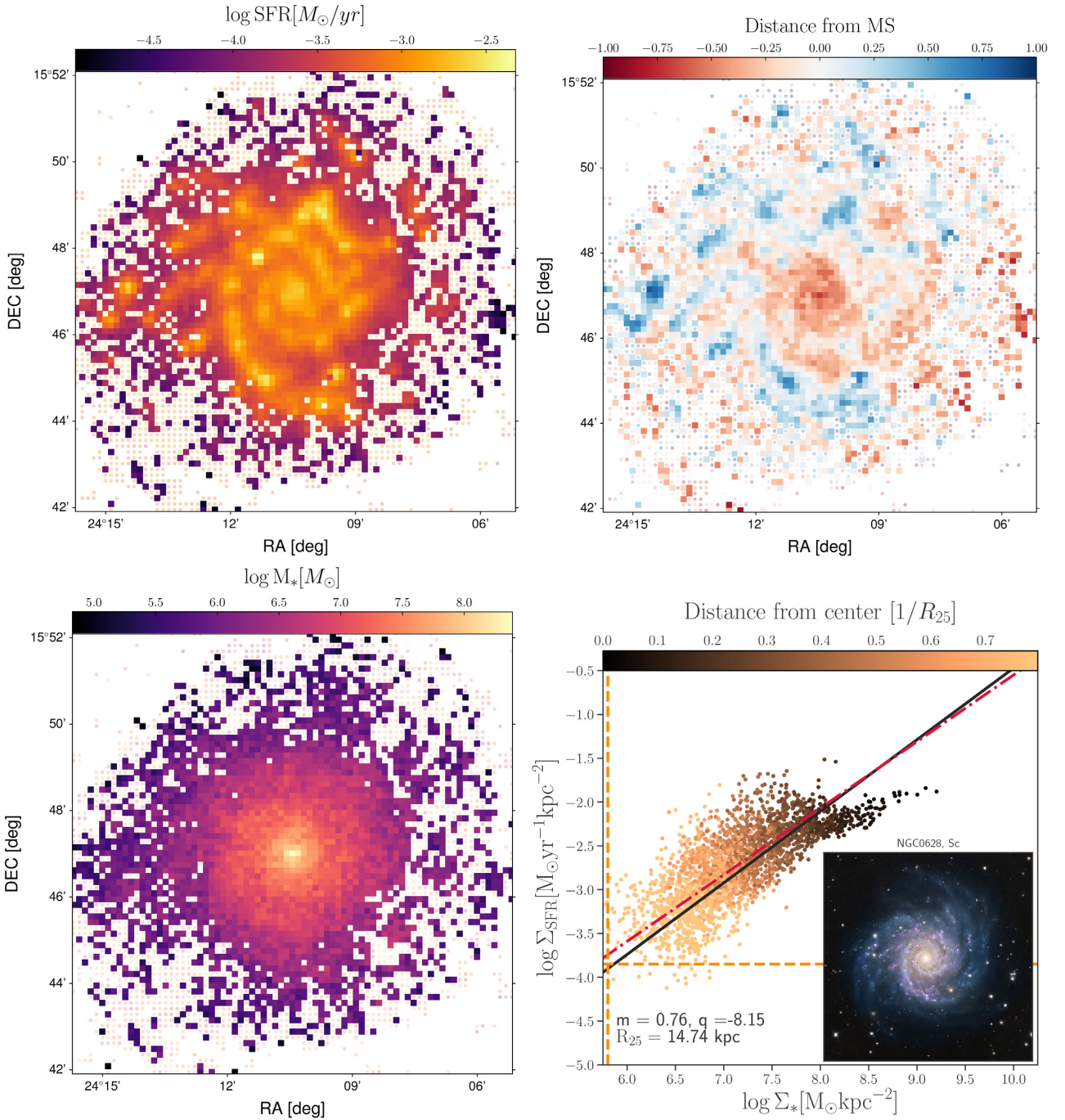
Figure 4. Summary plot for NGC 0628. The panels are organized as follows: *upper left*, the cells log SFR; *upper right*, the cells distance from the MS defined in Section 4; *lower left*, the cells log stellar mass; *lower right*, how the galaxy cells are positioned in the $\Sigma_\star - \Sigma_{SFR}$ plot, colour coded according to the distance from the galaxy centre in units of r_{25}. The black line is the (total fitted) MS, the red dashed line the ODR fit for the single galaxy points, the orange lines the sensitivity limits, and the inset an RGB image of the galaxy as observed in optical bands. In the first three panels, cells rejected for having a χ^2 over the threshold are shown as points. Results for the rest of the sample are reported in Appendix A.

25), while the colour-coded squares mark the cells with accepted χ^2 (as explained in Section 3.2). The black solid line in the bottom right panel of Fig. 4 and Figs A1–A7 is the MS relation of the combined sample, as explained in Section 4.1.

It is evident from the maps that the SFR traces the spiral pattern of each galaxy (as seen in the RGB image in the inset of the lower right panel). In addition, we can see that for almost all the sources the SFR distribution has a peak at the centre, as well

as several other peaks along the spiral arms. The stellar mass distribution is smoother and more centrally concentrated than as expected for an exponential mass distribution; in fact, according to the morphological classification of the galaxies as well as their RGB images, a bulge component is present in all our sources. The map of distance from the MS relation reveals that the spiral arms tend to lie above the relation for all the sources. The central bulge can be less (as in NGC 0628, NGC 3184, NGC 3938, and NGC
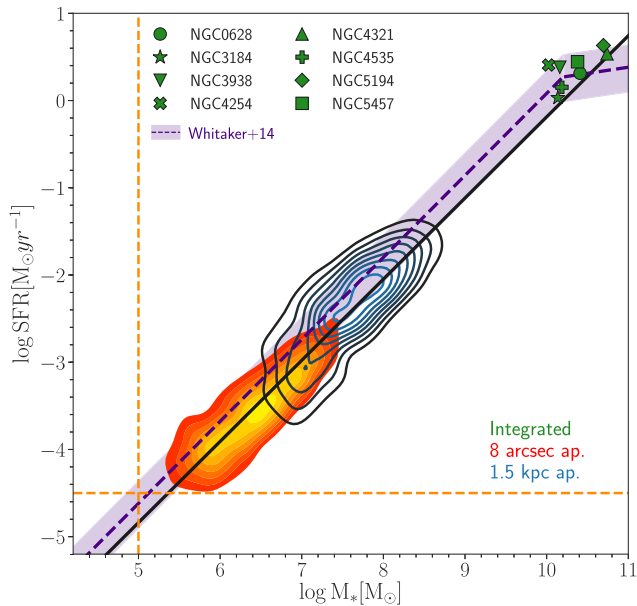
Figure 5. Sample properties evaluated in three different apertures. In green the integrated properties obtained fitting the available photometry in apertures enclosing the full galaxy emission. Marker size is as big as the data error bars. The blue and filled red contours are referred to cells of 1.5 kpc and 8 arcsec, respectively. The black line is the fit to the MS described by the 8 arcsec results. The purple dashed line is the MS relation from Whitaker et al. (2014) rescaled at $z \sim 0$, while the shaded area encloses the scatter of MS distribution we obtain (0.27 dex). The dashed orange lines are the $M_\star$ and SFR sensitivity limit.

5457) or more (as in NGC 4254, NGC 4321, and NGC 5194) star forming than the spiral arms. For those galaxies that have a 'red' bulge, a 'bending' of the MS relation is observed at the high $\Sigma_\star$ end, as the cells corresponding to the bulge component are also the more massive ones. It is worth noting that for the galaxies in our sample few spaxels would be considered passive (1 dex below the MS). This is a consequence of the sample selection, made of grand-design spirals. Also, due to the sample selection, there are no morphological trends in the $\log \Sigma_\star$–$\log \Sigma_{SFR}$ plane, i.e. in scatter from the global (or individual) MS or in slope. This aspect will be the subject of a future work, where we plan to extend the same analysis to all kind of morphological types within DustPedia.

The two galaxies that are infalling in the Virgo cluster, NGC 4254 and NGC 4321, show two peculiar characteristics. NGC 4254 is almost entirely made of cells that are located above the spatially resolved MS relation; indeed, this galaxy is the one that, according to its integrated properties, is located at the largest distance from the integrated MS relation (see Fig 5, X symbol), but still within the MS scatter. NGC 4321 and NGC 5194, instead, show the largest difference in slope with respect to the average MS relation. Interestingly, it also shows a second 'quenched' sequence below the MS, also observed in galaxies such as NGC 4535 and NGC 5194, and visible as a ring of red cells in Figs A4, A5, and A6.

4.1 Spatially resolved MS

In this section, we analyse the spatially resolved MS using two approaches: (1) by studying the distribution of the spatially resolved parameters in the $\log M_\star$–$\log$SFR plane, and (2) by analysing the distribution in the $\log \Sigma_\star$–$\log \Sigma_{SFR}$ plane. The first approach gives us the possibility to understand whether the integrated MS relations, computed using SFR and $M_\star$ estimated over the full

extent of galaxies, apply also at lower scales, thus hinting towards the existence of a universal relation at all scales. In Fig. 5 we show the $\log M_\star$–$\log$SFR plane and how the different cells in which we decompose the galaxies in our sample populate this plane. In particular, we show the results obtained using two different aperture sizes: 1.5 kpc (blue contours) and 8 arcsec (red-to-yellow gradient). We also plot, with green symbols, the integrated $\log M_\star$ and $\log$SFR values obtained via SED fitting on apertures that enclose the full galaxy. The orange dashed lines are the sensitivity thresholds, and correspond to the rms computed from the M_* and SFR maps on regions far away from the galaxy emission. We have also checked that the rms limit for the SFR is consistent with the one obtained from the SPIRE maps. The red solid line is our linear fit obtained including only data points over the sensitivity thresholds (orange dashed lines); it has a slope of 1.03 and intercept of −10.17. The contours referring to different spatial scales and the integrated quantities all lie along the same relation. The $\log M_\star$–$\log$SFR relation holds on a large variety of scales, from ones slightly over the size of the Giant Molecular Clouds (GMCs; $\sim$200 pc, Solomon et al. 1987) to the galaxy as a whole. This result is corroborated by the recent work of Chevance et al. (2019), showing that galactic star formation is driven by dynamical processes that are independent of the galaxy environment and are mostly governed by the GMC evolutionary cycling.

In Fig. 5 we also show the MS relation of Whitaker et al. (2014, dashed purple line), which was originally computed using integrated galaxy values in the redshift range [0.5:1.1] and for sources with stellar masses between 8.5 $\log M_\odot$ and 11.5 $\log M_\odot$. We also show the scatter of the MS relation derived for our sample (shaded region) at $z \sim 0$, as more evidence is mounting up for a non-evolution of the MS scatter with redshift (e.g. Popesso et al. 2019b). We rescale the Whitaker MS using the redshift evolution given in Whitaker et al. (2014). Interestingly, despite the different procedures and different stellar mass scales probed in the two works, the MS of Whitaker et al. (2014) is extremely consistent with the one found in this paper. This agreement clearly indicates the existence of the integrated MS relation as a consequence of a process that regulates the SF activity on small scales.

We then computed the MS relation in the $\log \Sigma_\star$–$\log \Sigma_{SFR}$ plane considering all the accepted cells coming from the eight galaxies. The fit, a log-linear relation $\log \Sigma_{SFR} = m \log \Sigma_\star + q$, is performed using EMCEE (Foreman-Mackey et al. 2013). Since we are dealing with a large number of points (from $\sim$3000 for 1.5 kpc apertures to $\sim$30 000 for 8 arcsec cells), we bin the data and perform linear fit on the binned data points (grey points in Fig. 6). Whenever binning, we discard the points falling below the sensitivity limits and consider only the ones above. The mass bins are built in two steps: first, we subdivide the $\log \Sigma_\star$ interval in 20 bins, each containing the same number of points. In order to probe the upper part of the MS (that otherwise would not have any binned points), we add a bin between $8.5 \leq \Sigma_\star < 9$ and one over 9 $M_\odot$ yr^{-1} kpc^{-2}. Within each bin, we compute the median $\Sigma_\star$ and Σ_{SFR}, while the error is taken as the standard deviation of the points inside the bin. We fit the binned data points with a log-linear relation. In Fig. 6 we report the 8 arcsec cell results for the sample, and the fit to the data (left-hand panel). The results of the fit are a slope of 0.82 ± 0.12 and intercept of -8.69 ± 0.97. As expected from Fig. 3, we tested that the MS obtained fitting the SFRs coming directly from MAGPHYS is consistent (almost identical) with this one.

Our slope is consistent with others in literature (see Section 4.2) that usually span the range 0.7–1.1 despite using different SFR tracers and different redshift and stellar mass ranges for the analysis (i.e. Pérez et al. 2013; Wuyts et al. 2013; Hemmati et al. 2014; Cano-
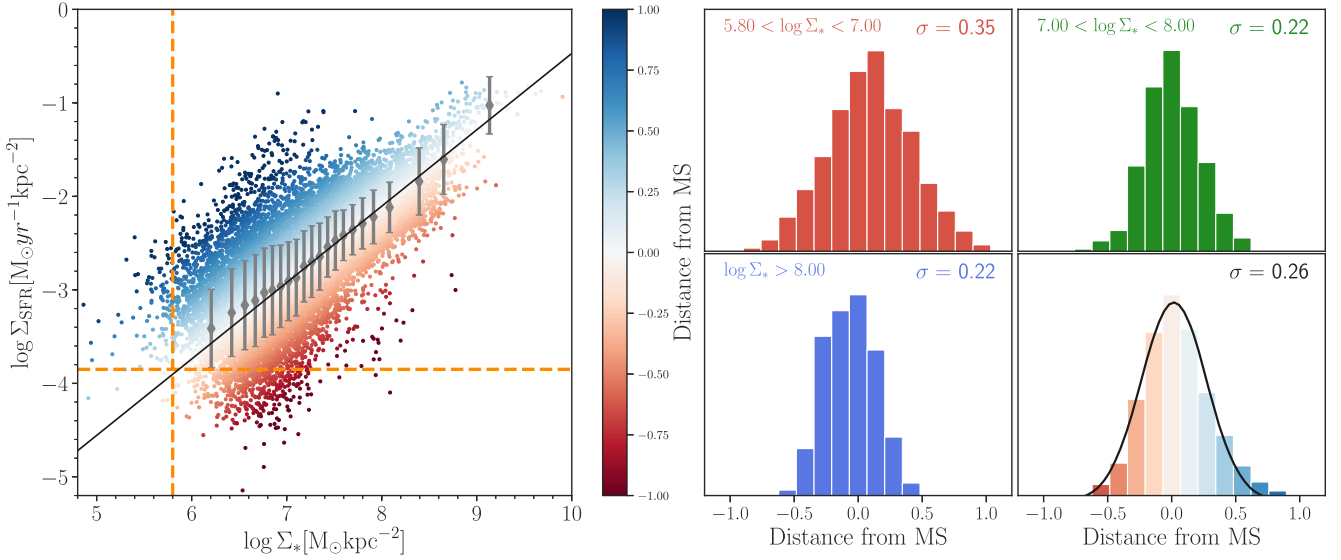
Figure 6. The fitted MS, and its scatter. *Left-hand panel:* 8 arcsec cell results for SFR surface density and stellar mass density, colour coded as a function of their distance from the MS. The orange dashes lines are the sensitivity limits. The MS (black solid line) is obtained as the linear fit of the grey data points. The error bars are the 1σ dispersion in each bin. *Right-hand panel:* distribution of distances from the MS, in three stellar mass bins (red, cyan, and blue, colour coded as in the left-hand panel). The σ values reported in each panel are obtained by fitting the distribution with a Gaussian. The scatter varies between 0.22 for the highest mass bin to 0.35 for the lowest mass bin.

Díaz et al. 2016; González Delgado et al. 2016; Abdurro'uf 2017, 2018; Hall et al. 2018; Cano-Díaz et al. 2019). It is worth noting that several of the literature works implement the orthogonal distance regression (ODR) method to find the location of the MS relation. If we perform an ODR fit on our results, we obtain a slope of 0.88 and an intercept of -9.05.

The right-hand panels of Fig. 6 are dedicated to the distribution scatter σ. We investigate if the scatter of the spatially resolved MS varies as a function of mass by dividing our sample in three mass bins, $5.8 \leq \log \Sigma_{\star} [\mathrm{M}_{\odot} \mathrm{yr}^{-1}] < 7.0$ (red histogram), $7.0 \leq \log \Sigma_{\star} [\mathrm{M}_{\odot} \mathrm{yr}^{-1}] < 8.0$ (green histogram), and $\log \Sigma_{\star} > 8.0 \mathrm{M}_{\odot}$ (blue histogram). The total scatter of the full sample (coloured histogram) is $\sigma = 0.26$. There are hints of a decreasing scatter with increasing stellar mass, from 0.35 to 0.23. Once again, these values fall within the typical ranges of 0.15–0.35 reported in the literature for the spatially resolved MS (Conselice et al. 2016; Magdis et al. 2016; Maragkoudakis et al. 2017; Hall et al. 2018). The importance of the scatter and the way it relates with the gas properties is explored in Morselli et al. (in prep).

Finally, we check that the results are consistent on different spatial scales. In Fig. 7 we compare the surface densities obtained for 8 arcsec cells (scales varying from 0.2 to 0.8 kpc) and 1.5 kpc cells. The black solid line is the MS fit to 8 arcsec data (though the fit to 1.5 kpc data leads to the same values well within the uncertainties), and orange lines the sensitivity thresholds. Both distributions follow the same relation, and occupy the same region of the plane, being clear how the retrieved surface density properties on bigger scales reflect the average surface density properties in enclosed smaller scales. The main differences, always in regions below the sensitivity thresholds, arise for galaxy regions where χ^2 criterion for 8 arcsec cells is not reached, as expected since 1.5 kpc cells have an intrinsically higher SNR for the SED points. The fact that the two realizations in different physical scales (sometimes even of an order of magnitude, i.e. NGC 5457) are almost overlapping tells us that the star formation laws still hold on physical scales lower than $\sim$500 pc.
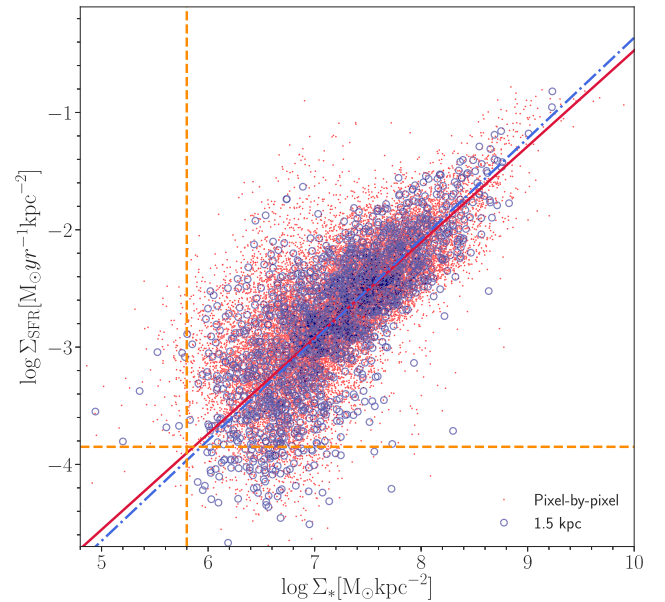

Figure 7. $\Sigma_{\star} - \Sigma_{\mathrm{SFR}}$ results for 8 arcsec (red points) and 1.5 kpc (blue circles) cells. The dashed lines are the sensitivity thresholds. It is clear how the results coming from the higher 1.5 kpc physical scale are the mean of the properties coming from the single cells inside them. Both data sets lead to the same linear relations (red line and blue dashed line, respectively), well within the uncertainties.

4.2 Comparison with other resolved star-forming MSs

In recent years, as already mentioned in the introduction, several works have analysed the spatially resolved MS of SFGs, thanks to the increased availability of IFS data. Surveys like MaNGA, CALIFA, and SAMI made it possible to obtain the SFR from the Hα luminosity, and to correct it for dust absorption through the Balmer decrement. The lack of information on the IR emission,
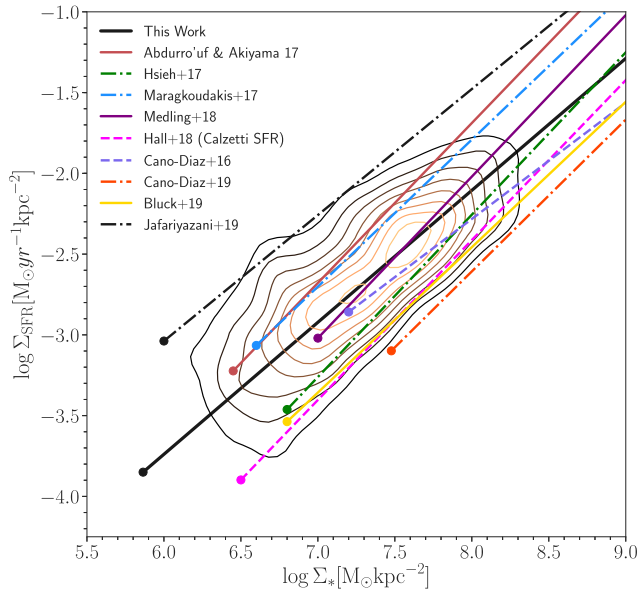
Figure 8. A comparison between our results (black-to-yellow contours encircling from 80 to 10 per cent of our data points, fitted by the solid black line) and a sample of resolved MS relations from the literature, respectively, with slopes reported in Table 2.. Each relation, which has been converted to a Chabrier (2003) IMF, and re-scaled to $z = 0$ (as described in the text), starts from the sensitivity limit reported in the study (or, if not, estimated from the relative data).

Table 2. Summary of the slopes quoted in the text, with associated SFR tracer.

Reference	Slope	SFR tracer
Cano-Díaz et al. (2016)	0.72	Hα
Abdurro'uf (2017)	0.99	SED fitting
Hsieh et al. (2017)	1.00	Hα
Maragkoudakis et al. (2017)	0.91	3.6 μm or 8.0 μm
Hall et al. (2018)	0.99	Hα + 24 μm
Medling et al. (2018)	1.00	Hα
Cano-Díaz et al. (2019)	0.94	Hα
Bluck et al. (2019)	0.90	Hα
This work	0.82	SED fitting

however, might prevent a comprehensive evaluation of the energetic budget in galaxies, as UV and optical tracers could underestimate a fraction of the obscured SFR (e.g. Rodighiero et al. 2014). In this section, we thus compare our panchromatic results with the spatially resolved MS relations obtained with data from CALIFA (Cano-Díaz et al. 2016), MaNGA (Hsieh et al. 2017; Bluck et al. 2019; Cano-Díaz et al. 2019), and SAMI (Medling et al. 2018). For completeness, we also compare our results with the MS relations of Abdurro'uf (2017), who performs pixel-by-pixel SED fitting to *GALEX* and SDSS photometry of local ($0.01 < z < 0.02$) massive spiral galaxies selected in the MPI-JHU (Max Planck Institute for Astrophysics-Johns Hopkins University), and of Hall et al. (2018), obtained for a sample of 355 nearby galaxies, with spatially resolved observations of Hα and mid-IR emission.

In Fig. 8 we show the spatially resolved MS relation of this work (solid black line) together with the relations mentioned above. To underline the depth of each study, in Fig. 8 we plot the relations as starting from the log $M_\star$ value above which 80 per cent of the corresponding data are located. The relations have

been homogenized in terms of IMF and cosmology, and rescaled to the median redshift of our sample, using the evolution in MS normalization of SFR $\propto (1 + z)^{2.88}$ (Whitaker et al. 2014).

The spatially resolved MS of Cano-Díaz et al. (2016, lavender dashed line) has been estimated from a sample of 306 galaxies with mixed morphologies at $0.005 < z < 0.03$, on spatial scales of 0.5–1.5 kpc. They find a slope of 0.72. Similarly, Hsieh et al. (2017) used 536 SFGs at $0.01 < z < 0.15$ from the MaNGA survey to obtain an MS relation on scales of ∼1 kpc (green dash–dotted line), obtaining a slope of 1.00 with the ODR fitting method. Recently, Cano-Díaz et al. (2019) updated the work of Hsieh et al. (2017) using ∼2000 galaxies from the MaNGA MPL-5 release ($0.01 < z < 0.15$) to probe the spatially resolved MS for a larger sample, again on spatial scales of ∼1.0 kpc. Their MS relation (orange dash–dotted line) has a slope of 0.94. Based on ∼3500 local galaxies in the SDSS-IV MaNGA-DR15 data, with SFRs coming from D4000 and Hα observations whenever available, Bluck et al. (2019, yellow line) obtain a slope of 0.90 on a data set of over 5 million spaxels. Maragkoudakis et al. (2017, blue dotted line) evaluate SFRs from IRAC 3.6 and 8.0 μm data at sub-kpc scales on a sample of 369 nearby galaxies ($z \sim 0.02$), obtaining a slope of 0.91. The MS of Medling et al. (2018, purple solid line) has been estimated from ∼800 galaxies in the SAMI Galaxy Survey at $z < 0.1$ and has a slope of 1.0. The MS relation of Hall et al. (2018, magenta dashed line) has a slope of 0.99, and was computed exploiting spatially resolved Hα observations of nearby galaxies within the Survey of Ionization in Neutral Gas Galaxies (SINGG) and WISE surveys (we report here the relation obtained using the SFR transformation of Calzetti et al. 2007). Finally, the MS of Abdurro'uf (2017, red line) has a slope of 0.99. All the reported spatially resolved MS slopes are reported in Table 2.

The immediate take-home information evident from Fig. 8 is that thanks to our multiwavelength approach we are able to probe regions of lower stellar mass surface densities (up to a factor of 10) compared to spectroscopic observations, bound to the sensitivity limit of the Hα line. This translates in the ability of sampling regions that are located further away from the galaxy centre, up to ∼2.5–3 effective radii (Re). While it is true that CALIFA galaxies have been selected in size so that most of them are fully sampled by the instrument field of view, the requirement to observe the Hα line with an SNR (S/N) > 3 in each resolution element translates in smaller radii within which the SFR can be efficiently computed, as it is clear from the different sensitivity limit. The same reasoning applies to the MS relations of Medling et al. (2018) and Cano-Díaz et al. (2019). On the other hand, Hall et al. (2018) reach lower Σ_{SFR} thanks to the combination of Hα and mid-IR data, but it has the drawback that low Σ_{SFR} only traces obscured SF.

The MS slope that we obtain is lower than the ones shown in Fig. 8 with the exception of the Cano-Díaz et al. (2016) relation. To exclude effects due to different fitting procedures, which can largely affect the MS slope and intercept, we also compute the relation using the ODR method, and we find a slope of 0.88. This value is still lower than the ones found in the works mentioned above, but it is important to underline that our relation was computed from eight galaxies against the hundreds of sources of other works. As there are strong galaxy-to-galaxy variations, it is important to apply our approach on a larger sample to carry out a more meaningful comparison with other works.

5 DISCUSSION AND CONCLUSIONS

In this paper, we have presented a new analysis of eight local face-on spirals, with the aim of understanding if the MS is a universal

relation holding also on sub-galactic scales. Other surveys of nearby galaxies have addressed this question, showing clear correlation between stellar masses and star formation per unit area, and to their gas content (Bigiel et al. 2008; Leroy et al. 2008; Casasola et al. 2015). By exploiting the publicly available photometric information of DustPedia in the UV-to-FIR spectral range, we have been able to perform a global SED fitting procedure that allowed us to simultaneously account for a careful evaluation of the obscured and unobscured SFR components, over the full optical radius, larger than what is obtained with optical IFS at similar redshifts. Our limited sample is restricted to the grand-design spirals with low inclination, large spatial extension, and regular spiral arm structures in DustPedia. This analysis has provided a total of tens of thousands of physical cells on typical scales of ∼0.5 kpc over very different internal galaxy environments (bulges, spiral arms, inter-arms regions, and outskirts). This set is thus well fit to study the secular evolution processes that regulate the star formation in local sources, dominated by rotationally supported systems (e.g. Förster Schreiber et al. 2009; Law et al. 2009; Glazebrook 2013; Wisnioski et al. 2015; Simons et al. 2017; Förster Schreiber et al. 2018; Übler et al. 2019).

Some individual galaxies show peculiar variation around the $\Sigma_{SFR}-\Sigma_\star$ relation presented in Fig. 6 (see the bottom right panels in Figs A1–A7). For example, NGC 3938 and NGC 4254 show an average enhancement of the SFR, which we interpret as a possible effect of the environment, as these two sources are located in the Ursa Major group and the Virgo cluster, respectively. Other galaxies, in particular NGC 0628, show a prominent bulge feature appearing as a narrow distribution at the highest stellar mass densities. Indeed, we already mentioned that at the lowest stellar mass densities (i.e. at large galactocentric distances) in few sources we have identified a cloud of cells deviating from the main relation towards lower SFR, at a fixed stellar mass (NGC 4321 is the cleanest example). Such distributions are circularly distributed in the outer parts of the galaxies, out of the regions spanned by the dynamical interaction of the spiral arms. It is still to be understood if this is associated with an older population migrated out of the disc, or if it is the remnant of external accretion through, for example, minor merging. Finally, only NGC 5457 reveals strong mini-starbursts inside the spiral arms (i.e. regions well elevated above the MS, by a factor larger than 10–100 times at a fixed mass density).

In any case, the combination of all the eight galaxies demonstrates the existence of a universal relation, as the deviation of single sources is well within the global scatter of ∼0.27 dex (see Section 4.3). We have then demonstrated that such a relation holds at different galaxy scales, supporting the interpretation from other surveys that the SFR is regulated by local processes of gas-to-stars conversion happening at GMC scales of the order of a few hundred pc. With respect to other works, we have, however, provided evidence that such *secular regulation* keeps to apply at the farthest galactocentric distances, where the optical disc is still influenced by the density wave motions, originating the spiral arms.

This work defines an accurate locus in the $\Sigma_{SFR}-\Sigma_\star$ plane, constrained by observed distributions covering 3 dex in the parameter space. Such a definition of the spatially resolved MS in local disc galaxies represents a valuable reference for future comparison to different galaxy morphological types adopting a similar panchromatic approach. Indeed, there are indications that galaxy morphology plays an important role in characterizing the spatially resolved MS relation, especially its scatter (e.g. González Delgado et al. 2016; Cano-Díaz et al. 2019). Maragkoudakis et al. (2017) observe a decrease in the spatially resolved MS relation from late-type to early-type spirals, while the scatter remains constant. Other works do not find a similar connection (Hall et al. 2018).

These examples show the importance of extending the analysis performed in this work to a larger sample of galaxies encompassing different morphologies.

In the second paper of this series, we will exploit this reference sample to study if and how the distance to the resolved MS is connected to the total (atomic and molecular) gas content (Morselli et al., in prep.).

6 SUMMARY

The star-forming MS is a well-studied tight relation between stellar masses and SFRs, observed up to $z \sim 6$, over a great variety of environments and morphologies, both globally, counting galaxies as a whole, and locally, resolving physical properties in single galaxy regions. In this work, we perform spatially resolved SED fitting in a sample of eight local grand-design spirals taken from the DustPedia archive and we use the outputted maps of stellar mass and SFR (see the appendix) to analyse the spatially resolved MS of SFGs on scales spanning the range between 0.4 and 1.5 kpc. We summarize here our main findings:

(i) When considering the eight galaxies together, we obtain a spatially resolved MS with a slope of 0.82 and an intercept of −8.69. When fitting the data with the ODR method, we obtain a slope and an intercept of 0.88 and −9.05, respectively. This relation holds on different scales, from sub-galactic to galactic;

(ii) The local spatially resolved MS is consistent with the evolutionary (from high-z) low-mass relation, thus proving its universality across cosmic time. This is a crucial point to validate the integrated information on individual galaxies at high redshifts;

(iii) We have overtaken the limits of all the spectroscopic resolved emission line studies, based mainly on Hα and Balmer decrement corrections for dust extinction. The sensitivities of these surveys do not sample the lowest $M_\star$ and SFR as we do with a multiwavelength photometric approach, allowing us to probe the outermost regions of galaxies.

We plan to extend this analysis on different morphological types inside the DustPedia sample, while improving the SED fitting pipeline to investigate star formation histories of resolved galaxy regions. We will also link these results with existing gas observations (i.e. CO, H_2, and C II) to further understand the role of secular evolution in galaxies.

REFERENCES

Abdurro'uf A. M., 2017, MNRAS, 469, 2806
Abdurro'uf A. M., 2018, MNRAS, 479, 5083
Aniano G., Draine B. T., Gordon K. D., Sandstrom K., 2011, PASP, 123, 1218
Bell E. F., Kennicutt R. C., Jr, 2001, ApJ, 548, 681
Berta S. et al., 2013, A&A, 551, A100
Bigiel F., Leroy A., Walter F., Brinks E., de Blok W. J. G., Madore B., Thornley M. D., 2008, AJ, 136, 2846
Bluck A. F. L., Maiolino R., Sánchez S. F., Ellison S. L., Thorp M. D., Piotrowska J. M., Teimoorinia H., Bundy K. A., 2019, MNRAS, 485, 2839
Bradley L. et al., 2019, Astropy/photutils: v0.6. available at: https://doi.org/10.5281/zenodo.2533376
Brammer G. B. et al., 2012, ApJS, 200, 13
Bruzual G., Charlot S., 2003, MNRAS, 344, 1000
Bundy K. et al., 2015, ApJ, 798, 7
Calzetti D. et al., 2007, ApJ, 666, 870
Camps P., Baes M., 2015, Astron. Comput., 9, 20
Cano-Díaz M. et al., 2016, ApJ, 821, L26
Cano-Díaz M., Ávila-Reese V., Sánchez S. F., Hernández-Toledo H. M., Rodríguez-Puebla A., Boquien M., Ibarra-Medel H., 2019, MNRAS, 488, 3929
Casasola V., Hunt L., Combes F., García-Burillo S., 2015, A&A, 577, A135
Chabrier G., 2003, PASP, 115, 763
Chang Y.-Y., van der Wel A., da Cunha E., Rix H.-W., 2015, ApJS, 219, 8
Charlot S., Fall S. M., 2000, ApJ, 539, 718
Chevance M. et al., 2019, MNRAS, in press
Chrimes A. A., Stanway E. R., Levan A. J., Davies L. J. M., Angus C. R., Greis S. M. L., 2018, MNRAS, 478, 2
Clark C. J. R. et al., 2018, A&A, 609, A37
Conselice C. J., Wilkinson A., Duncan K., Mortlock A., 2016, ApJ, 830, 83
Corwin Harold G. J., Buta R. J., de Vaucouleurs G., 1994, AJ, 108, 2128
Croom S. M. et al., 2012, MNRAS, 421, 872
da Cunha E., Charlot S., Elbaz D., 2008, MNRAS, 388, 1595
da Cunha E., Charmandaris V., Díaz-Santos T., Armus L., Marshall J. A., Elbaz D., 2010, A&A, 523, A78
Daddi E. et al., 2007, ApJ, 670, 156
Davies J. I. et al., 2017, PASP, 129, 044102
0000000de Vaucouleurs G., de Vaucouleurs A., Corwin Herold G. J., Buta R. J., Paturel G., Fouque P., 1991, Third Reference Catalogue of Bright Galaxies, Vol. 82, Sky and Telescope, p. 621
Driver S. P. et al., 2018, MNRAS, 475, 2891
Elbaz D. et al., 2007, A&A, 468, 33
Foreman-Mackey D., Hogg D. W., Lang D., Goodman J., 2013, PASP, 125, 306
Förster Schreiber N. M. et al., 2009, ApJ, 706, 1364
Förster Schreiber N. M. et al., 2018, ApJS, 238, 21
Glazebrook K., 2013, Publ. Astron. Soc. Aust., 30, e056
González Delgado R. M. et al., 2016, A&A, 590, A44
Grogin N. A. et al., 2011, ApJS, 197, 35
Hall C., Courteau S., Jarrett T., Cluver M., Meurer G., Carignan C., Audcent-Ross F., 2018, ApJ, 865, 154
Hayward C. C., Smith D. J. B., 2015, MNRAS, 446, 1512
Hemmati S. et al., 2014, ApJ, 797, 108
Hsieh B. C. et al., 2017, ApJ, 851, L24
Jafariyazani M., Mobasher B., Hemmati S., Fetherolf T., Khostovan A. A., Chartab N., 2019, ApJ, 887, 204
Kennicutt R. C., Jr, 1998, ApJ, 498, 541
Khoperskov S. A., Vasiliev E. O., 2017, MNRAS, 468, 920
Koekemoer A. M. et al., 2011, ApJS, 197, 36

Kravtsov A. V., 2003, ApJ, 590, L1
Law D. R., Steidel C. C., Erb D. K., Larkin J. E., Pettini M., Shapley A. E., Wright S. A., 2009, ApJ, 697, 2057
Leroy A. K., Walter F., Brinks E., Bigiel F., de Blok W. J. G., Madore B., Thornley M. D., 2008, AJ, 136, 2782
Lin L. et al., 2017, ApJ, 851, 18
Magdis G. E. et al., 2016, MNRAS, 456, 4533
Makarov D., Prugniel P., Terekhova N., Courtois H., Vauglin I., 2014, A&A, 570, A13
Maragkoudakis A., Zezas A., Ashby M. L. N., Willner S. P., 2017, MNRAS, 466, 1192
Martis N. S., Marchesini D. M., Muzzin A., Stefanon M., Brammer G., da Cunha E., Sajina A., Labbe I., 2019, ApJ, 882, 65
Medling A. M. et al., 2018, MNRAS, 475, 5194
Meurer G. R. et al., 2006, ApJS, 165, 307
Morrissey P. et al., 2007, ApJS, 173, 682
Morselli L., Popesso P., Erfanianfar G., Concas A., 2017, A&A, 597, A97
Noeske K. G. et al., 2007, ApJ, 660, L47
Oliver S. et al., 2010, MNRAS, 405, 2279
Pannella M. et al., 2009, ApJ, 698, L116
Pearson W. J. et al., 2018, A&A, 615, A146
Peng Y., Maiolino R., Cochrane R., 2015, Nature, 521, 192
Pérez E. et al., 2013, ApJ, 764, L1
Pilbratt G. L. et al., 2010, A&A, 518, L1
Planck Collaboration XIII, 2016, A&A, 594, A13
Poggianti B. M. et al., 2017, ApJ, 844, 48
Popesso P. et al., 2019a, MNRAS, 483, 3213
Popesso P. et al., 2019b, MNRAS, 490, 5285
Renzini A., Peng Y.-j., 2015, ApJ, 801, L29
Rodighiero G. et al., 2011, ApJ, 739, L40
Rodighiero G. et al., 2014, MNRAS, 443, 19
Rosales-Ortega F. F., Sánchez S. F., Iglesias-Páramo J., Díaz A. I., Vílchez J. M., Bland-Hawthorn J., Husemann B., Mast D., 2012, ApJ, 756, L31
Saintonge A. et al., 2016, MNRAS, 462, 1749
Sánchez S. F. et al., 2012, A&A, 538, A8
Sánchez S. F. et al., 2013, A&A, 554, A58
Sánchez S. F., 2019, preprint (arXiv:1911.06925)
Santini P. et al., 2009, A&A, 504, 751
Santini P. et al., 2017, ApJ, 847, 76
Sargent M. T., Bethermin M., Daddi E., Elbaz D., 2012, ApJ, 747, L31
Schreiber C. et al., 2015, A&A, 575, A74
Schruba A., Leroy A. K., Walter F., Sand strom K., Rosolowsky E., 2010, ApJ, 722, 1699
Shivaei I., Reddy N. A., Steidel C. C., Shapley A. E., 2015, ApJ, 804, 149
Simons R. C. et al., 2017, ApJ, 843, 46
Skrutskie M. F. et al., 2006, AJ, 131, 1163
Smith D. J. B., Hayward C. C., 2015, MNRAS, 453, 1597
Smith D. J. B., Hayward C. C., 2018, MNRAS, 476, 1705
Smith D. J. B. et al., 2012, MNRAS, 427, 703
Sobral D., Best P. N., Smail I., Mobasher B., Stott J., Nisbet D., 2014, MNRAS, 437, 3516
Solomon P. M., Rivolo A. R., Barrett J., Yahil A., 1987, ApJ, 319, 730
Speagle J. S., Steinhardt C. L., Capak P. L., Silverman J. D., 2014, ApJS, 214, 15
Steinhardt C. L. et al., 2014, ApJ, 791, L25
Tacchella S., Dekel A., Carollo C. M., Ceverino D., DeGraf C., Lapiner S., Mandelker N., Primack J. R., MNRAS, 2016, 458, 242
Viaene S. et al., 2014, A&A, 567, A71
Vulcani B. et al., 2019, MNRAS, 488, 1597
Werner M. W. et al., 2004, ApJS, 154, 1
Whitaker K. E. et al., 2014, ApJ, 795, 104
Williams T. G., Gear W. K., Smith M. W. L., 2018, MNRAS, 479, 297
Wisnioski E. et al., 2015, ApJ, 799, 209
Wright E. L. et al., 2010, AJ, 140, 1868
Wuyts S.et al.,2011, ApJ, 742, 96
Wuyts S. et al., 2013, ApJ, 779, 135
York D. G. et al., 2000, AJ, 120, 1579
Übler H. et al., 2019, ApJ, 880, 48

APPENDIX A: GALAXY-BY-GALAXY RESULTS

In this appendix, we present the individual galaxy-by-galaxy results, reporting the SFR and stellar mass maps, along with a map measuring the distance from the fitted MS (blue points towards starburst and red points towards quenched ones). In the lower left panel, we report the results on the $M_\star$–SFR plane, with fitted (total) MS in black and the one fitting the lone galaxy results.
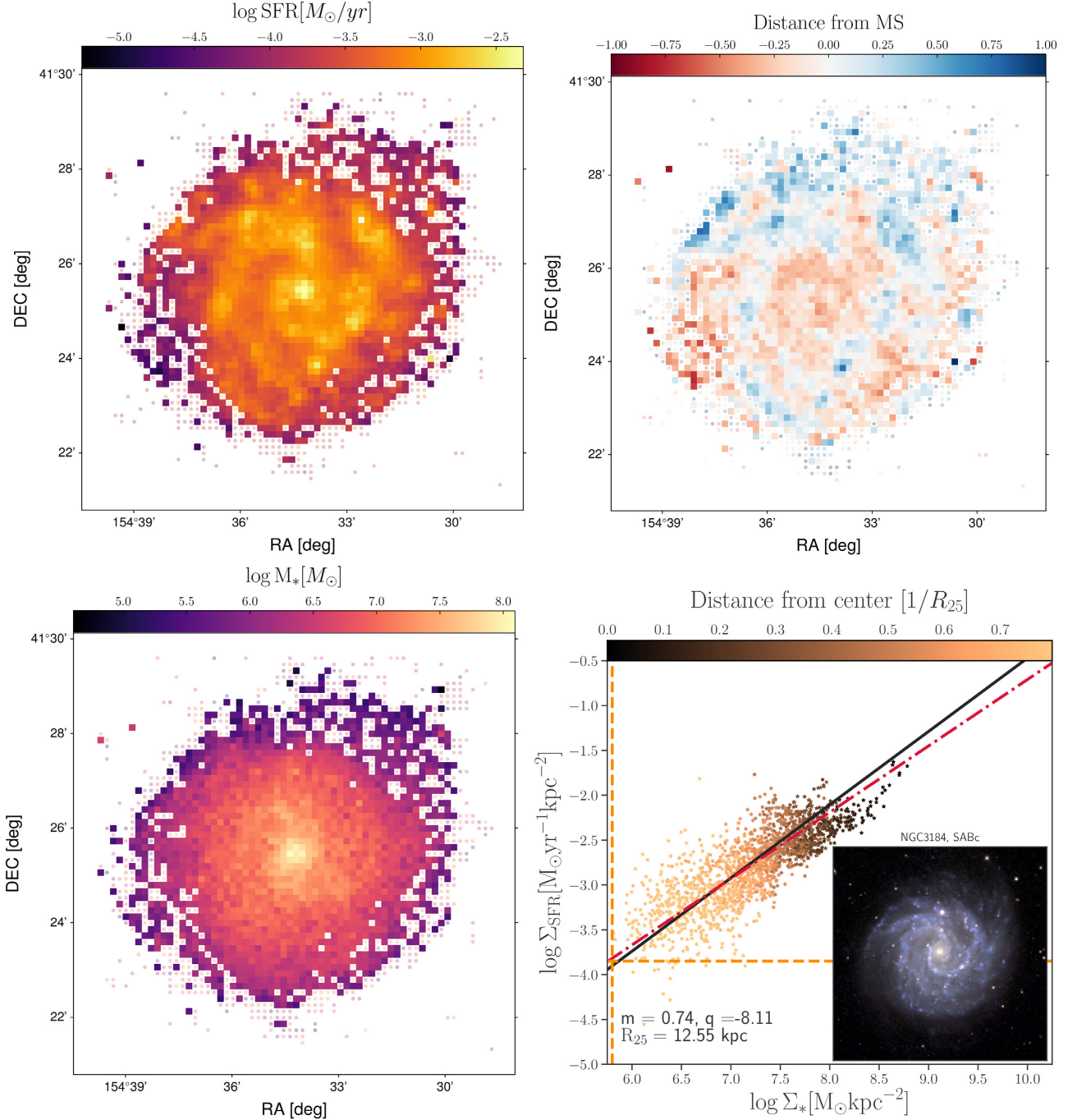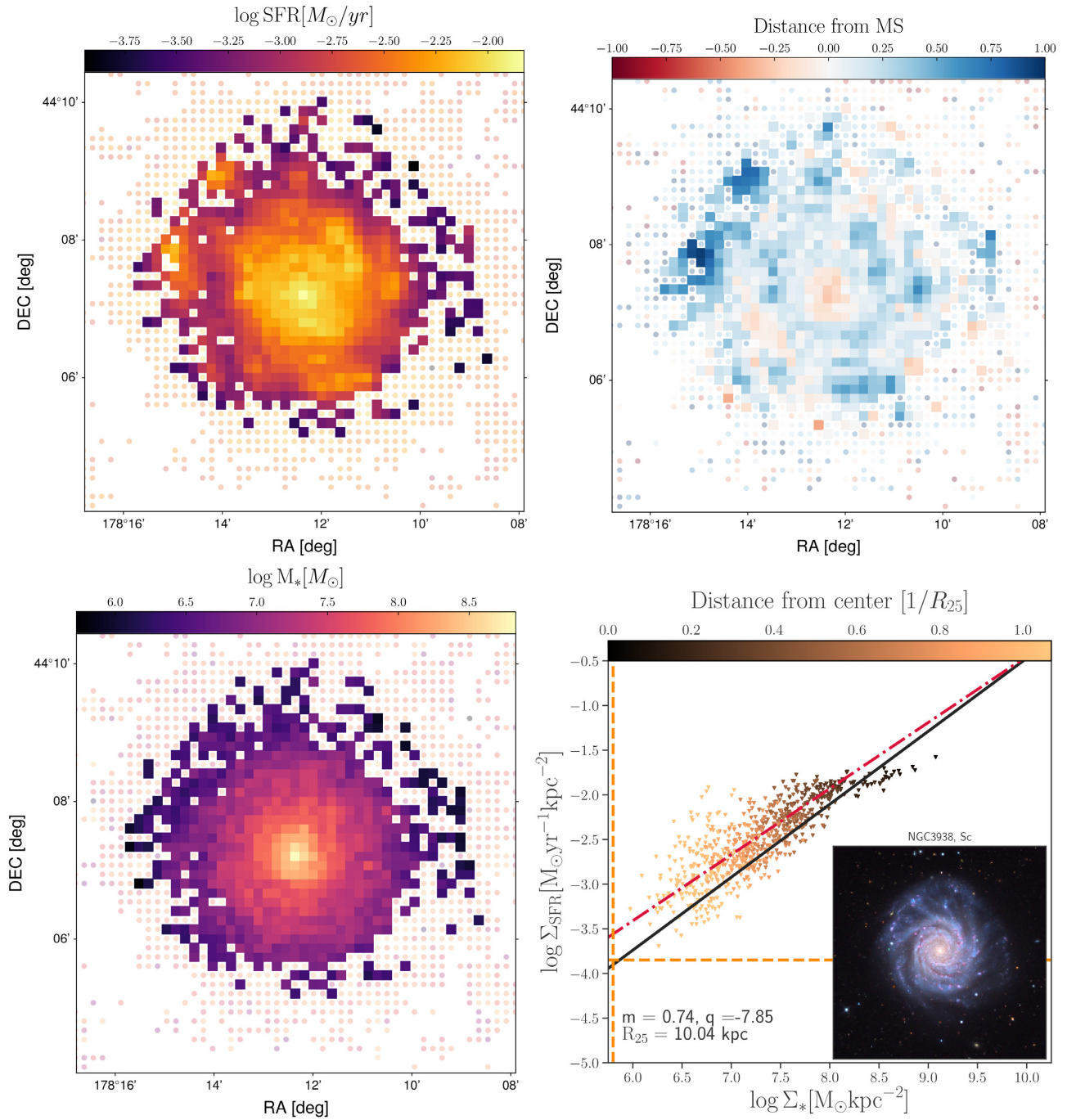
Figure A1. Same as Fig. 4, for NGC 3184.

Figure A2. Same as Fig. 4, for NGC 3938.
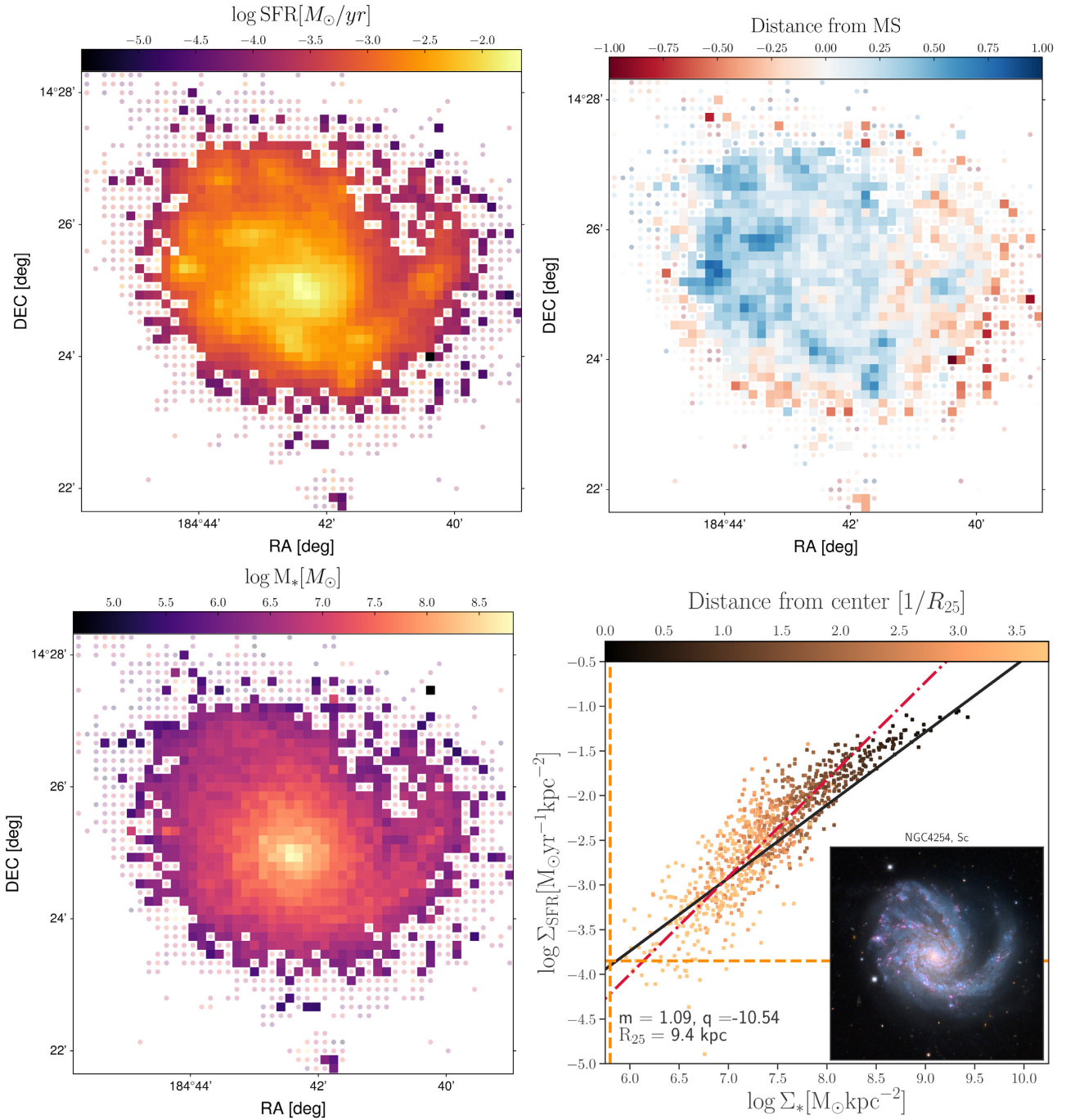
Figure A3. Same as Fig. 4, for NGC 4254.
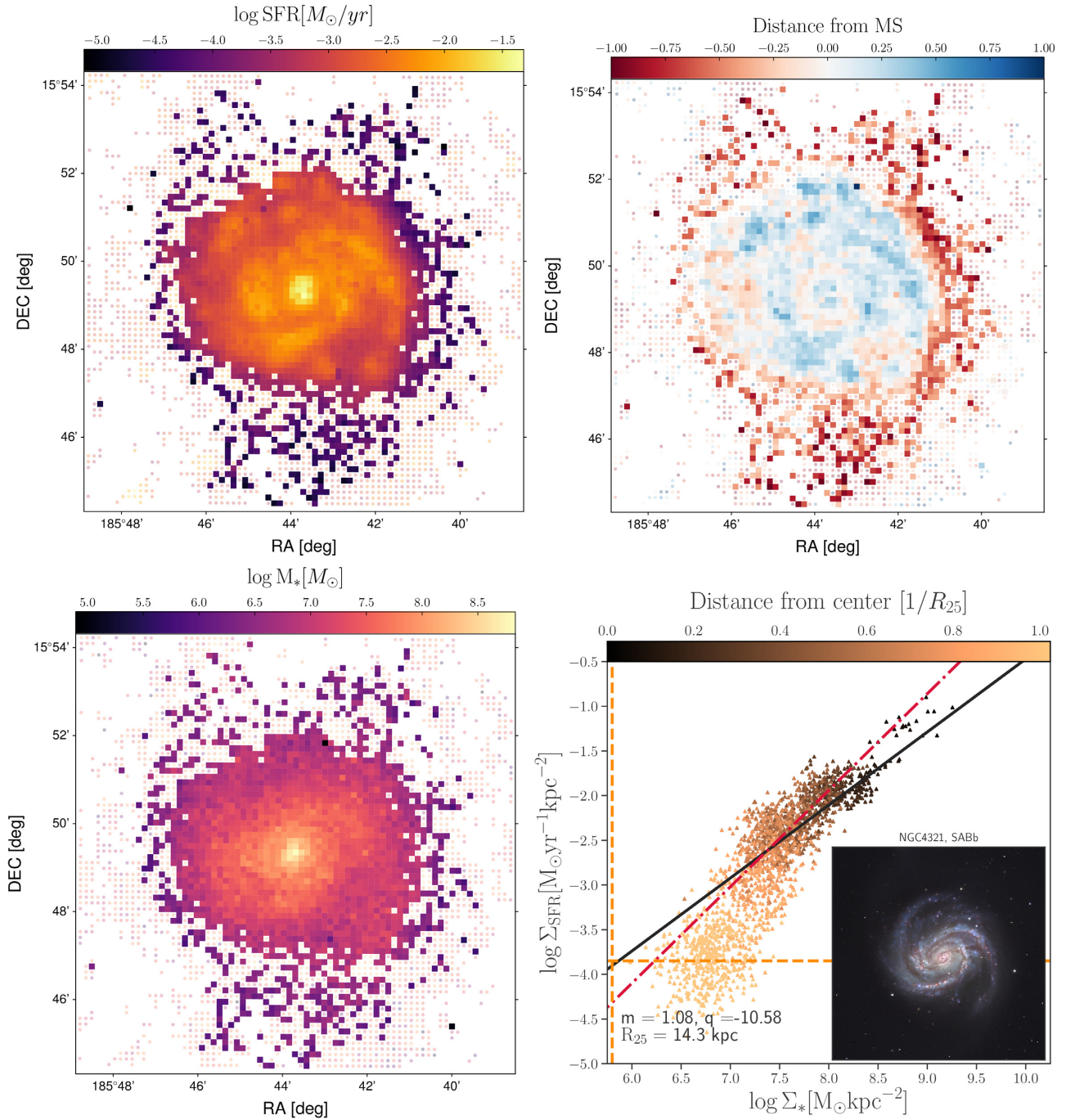
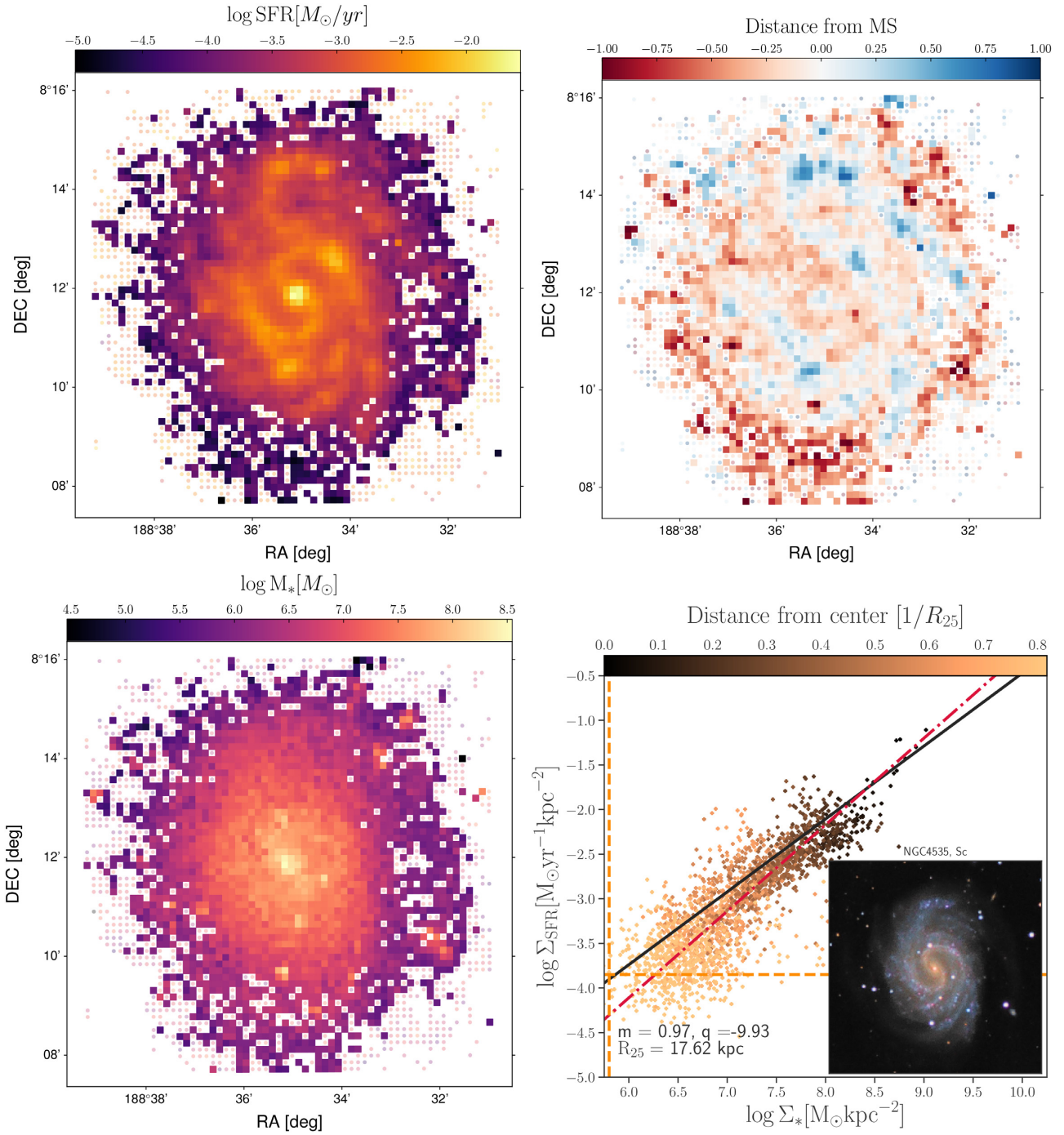**Figure A4.** Same as Fig. 4, for NGC 4321.
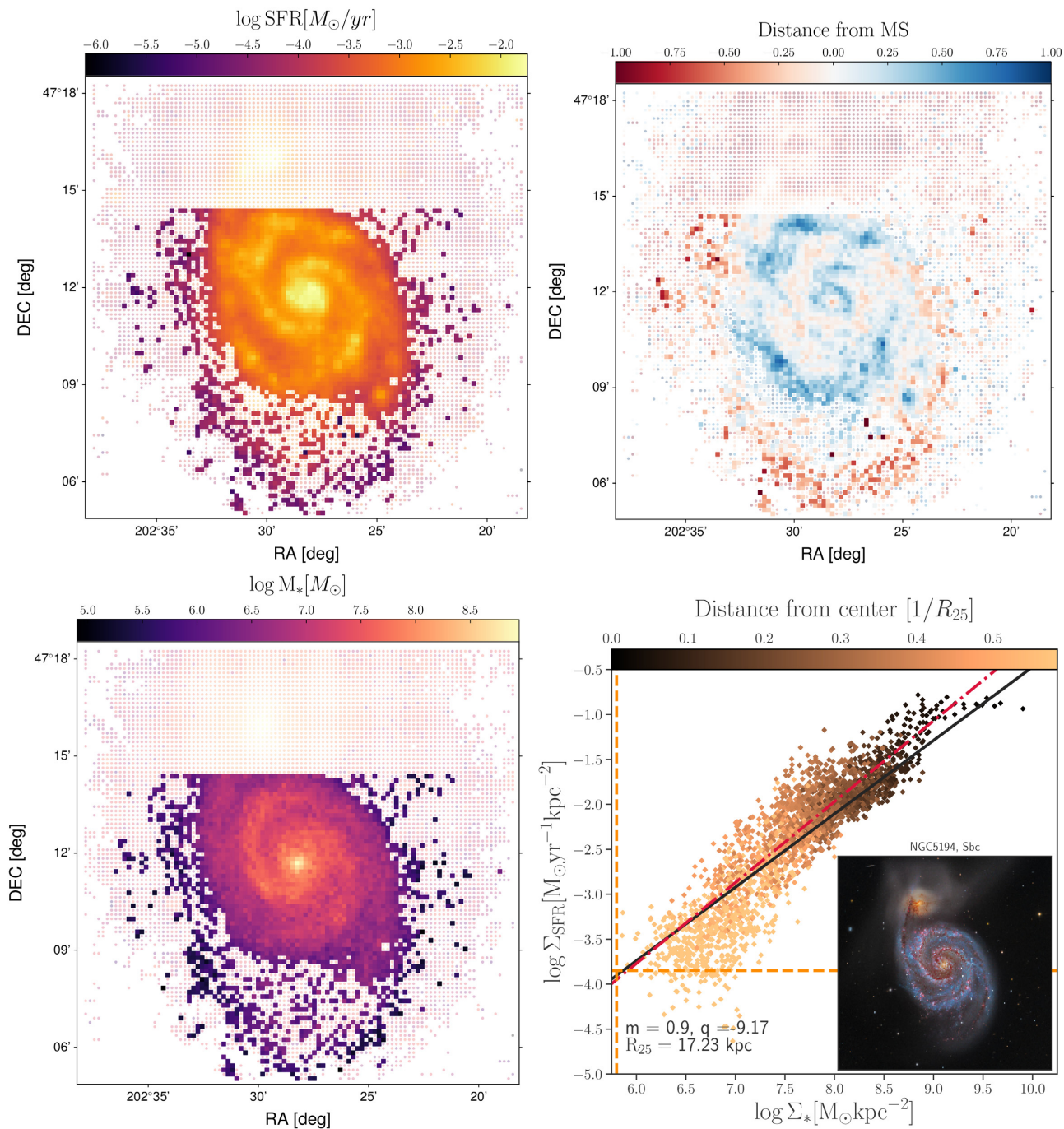
Figure A5. Same as Fig. 4, for NGC 4535.

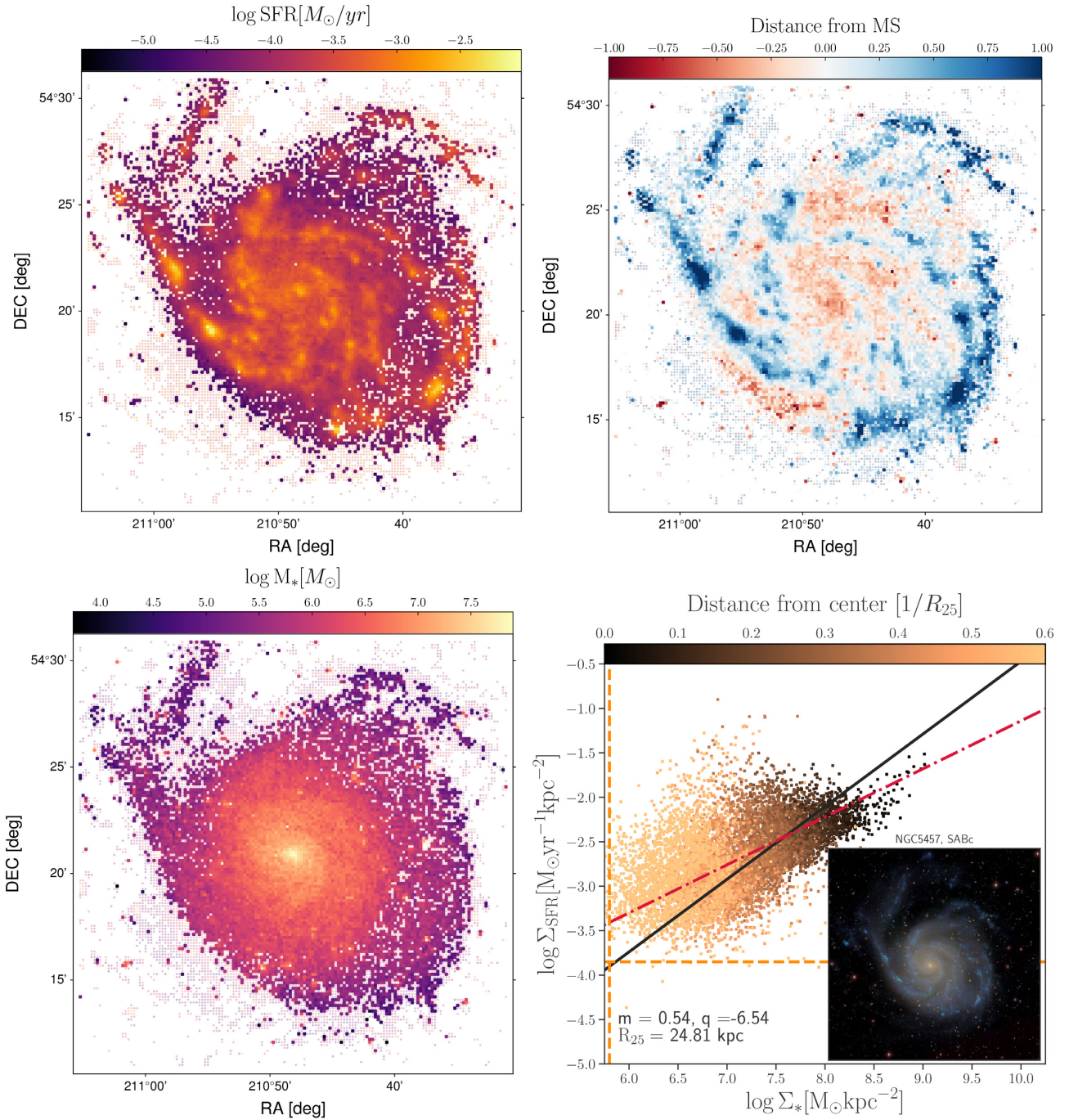**Figure A6.** Same as Fig. 4, for NGC 5194.

Figure A7. Same as Fig. 4, for NGC 5457.

This paper has been typeset from a TEX/LATEX file prepared by the author.